# Cretaceous thermal evolution of the closing Neo-Tethyan realm revealed by multi-method petrochronology

Regina Holtmann, Jesus Muñoz-Montecinos, Samuel Angiboust, Aitor Cambeses, Guillaume Bonnet, Allison Brown, Besim Dragovic, Zeynab Gharamohammadi, Mathieu Rodriguez, Johannes Glodny, et al.

## To cite this version:

Regina Holtmann, Jesus Muñoz-Montecinos, Samuel Angiboust, Aitor Cambeses, Guillaume Bonnet, et al.. Cretaceous thermal evolution of the closing Neo-Tethyan realm revealed by multi-method petrochronology. Lithos, 2022, 422-423, pp.106731. 10.1016/j.lithos.2022.106731 . hal-04841343

HAL Id: hal-04841343
https://hal.science/hal-04841343v1

Submitted on 16 Dec 2024

# Cretaceous thermal evolution of the closing Neo-Tethyan realm revealed by multi-method petrochronology

**Regina Holtmann[1], Jesús Muñoz-Montecinos[1,2], Samuel Angiboust[1,3*], Aitor Cambeses[2], Guillaume Bonnet[4,5], Allison Brown[6], Besim Dragovic[6], Zeynab Gharamohammadi[7], Mathieu Rodriguez[8], Johannes Glodny[9], Ali Kananian[7], Philippe Agard[5]**

[1] *Université de Paris, Institut de Physique du Globe de Paris, CNRS, F-75005 Paris, France*
[2] *Department of Mineralogy and Petrology, Faculty of Sciences, University of Granada, Campus Fuentenueva s/n, 18002 Granada, Spain*
[3] *ENS Lyon, University of Lyon, CNRS, LGL-TPE, 46 Allée d'Italie, F-69007 Lyon, France*
[4] *Department of Earth Science, Earth Research Institute, University of California, Santa Barbara, CA, USA*
[5] *Institut des Sciences de la Terre de Paris, Sorbonne Université, Paris, France*
[6] *School of the Earth, Ocean and Environment, University of South Carolina, Columbia, SC, USA*
[7] *School of Geology, College of Science, University of Tehran, Tehran, Iran*
[8] *Laboratoire de Géologie, Ecole normale supérieure, PSL research university, CNRS UMR 8538, 24 rue Lhomond, 75005 Paris, France*
[9] *GFZ German Research Centre for Geosciences, Potsdam, Germany*

*: corresponding author *(samuel.angiboust@ens-lyon.fr)*

## ABSTRACT

A Cretaceous paleo-accretionary wedge, the Ashin Complex, now exposed along the Zagros suture zone in southern Iran, exhibits mafic, metasedimentary and subordinate ultramafic lithologies. Field, geochemical and petrological observations point to an anomalous high-temperature event that gave rise to the formation of peritectic (trondhjemitic) melts associated with restitic garnet-bearing amphibolites. Lu-Hf isotopic dating of centimetre-sized garnet in amphibolite-facies metasediments yielded a crystallization age of 113.10 ± 0.36 Ma, possibly representing the age of prograde to near-peak metamorphic conditions. SHRIMP U-Th-Pb zircon dating from trondhjemitic leucosomes yields crystallization ages of 104 ± 1 Ma, interpreted as the age of the temperature peak, which occurred in the upper amphibolite-facies (c. 650-680 °C at 1.1-1.3 GPa), according to thermodynamic modelling and Ti-in-zircon thermometry. Rutile crystals from two leucosomes yield Zr-in-rutile temperatures in the range of 580-640 °C and a LA-ICP-MS U-Pb age range from 85 to 112 Ma, interpreted as a consequence of partial re-equilibration during incipient cooling. A late static recrystallization event is indicated by the presence of sodic-calcic clinopyroxene, sodic amphibole, Si-rich phengite, titanite overgrowths after rutile and lawsonite within former leucosomes and late fractures. This mineral assemblage is a typical blueschist-facies (high pressure-low temperature) paragenesis and is interpreted as reflecting long-term isobaric cooling that occurred until the end of the Cretaceous as a consequence of increasing slab thermal age. This first report of a melting event in the Zagros paleo-accretionary wedge reveals the presence of a transient, abnormally high thermal gradient of c. 18 °C/km that occurred at c. 105-113 Ma. We speculate that this could be explained by the subduction of a thermal anomaly such as a seamount chain, a transform fault system or, more likely, a spreading ridge under the southern Iranian margin. Indeed, paleogeographic reconstructions of the Tethyan realm suggest the entrance of the Northern Tethyan basin ridge into the subduction zone shortly after 120 Ma.

## 1. INTRODUCTION

Critical information on past geodynamic processes and regional scale paleogeographic reconstructions can be derived studying ancient convergent margins and accretionary wedges (e.g. Stern, 2002; Rossetti et al., 2017). A number of previous studies have demonstrated that paleo-accretionary wedges do record long-term fluctuations of the subduction thermal gradient over geological timescales (Grove & Bebout, 1995; García-Casco et al., 2008; Lázaro et al, 2009; Angiboust et al., 2018). Subduction initiation, known to be marked by a hot thermal environment during the first millions of years of subduction activity (Guilmette et al., 2018; Pourteau et al., 2019), is invariably followed by a secular cooling of the subduction thermal gradient as convergence proceeds to reach a nearly steady-state regime (e.g. Anczkiewicz et al., 2004; Angiboust et al., 2016). However, subduction zone thermal structure is known to be rather unstable over millions of years. Several processes such as convergence rate decrease, slab dip flattening or the subduction of a thermal anomaly (e.g. a ridge, a triple junction) can leave an imprint permanently recorded in the rock record of ancient margins or volcanic arc chemical compositions (e.g. Lagabrielle et al., 2000).

Only a few areas are witnesses of the long-term thermal evolution of the Neo-Tethyan realm in Asia during Mesozoic times (e.g. Angiboust et al., 2016; Pourteau et al., 2019). Meta-ophiolitic remnants from this oceanic realm are volumetrically scarce (e.g. Agard et al., 2006; Omrani et al., 2008; Burg, 2018; Saccani et al., 2018) and when present, they do not commonly record a time window long enough to shed light on the long-term thermal evolution of the subduction zone. The c. 3000 km-long Zagros belt in southern Iran, unlike most classical subduction-collisional Alpine belts, does not exhibit large exposures of paleo-accretionary rocks despite an enduring subduction history (c. 180-35 Ma; Berberian & King, 1981; Sengör et al., 1988; McCall, 1997). Remnants from the deep Neo-Tethyan paleo-accretionary wedge are particularly well-preserved in the Hajiabad-Esfandagheh region (**Figs.1A** and **B**) where slivers of oceanic lithosphere origin have been accreted against the Sanandaj-Sirjan zone (SaSZ). The SaSZ has been interpreted as the thinned SW margin of the Eurasian continental plate (e.g. Alavi, 1994; Agard et al., 2006; Hassanzadeh & Wernicke, 2016). Previous studies have demonstrated that metamorphic rocks in the Hajiabad-Esfandagheh region form an antiformal nappe-stack that has been metamorphosed during the Upper Cretaceous under a thermal gradient compatible with a subduction zone environment (7-10 °C/km; e.g. Agard et al., 2006; Angiboust et al., 2016; Muñoz-Montecinos et al., 2021). This led to the formation of blueschist-facies rocks, occasionally overprinting higher temperature amphibolite-facies material (the Ashin garnet micaschists described in Agard et al., 2006). The Ashin complex, which represents the structurally highest sliver of the nappe-stack (Angiboust et al., 2016), exhibits a multi-stage metamorphic history with a spread in metamorphic ages ranging between c. 120 Ma to c. 79 Ma (K-Ar: Ghasemi et al., 2002; $^{40}$Ar-$^{39}$Ar: Agard et al., 2006; Rb-Sr: Angiboust et al., 2016 and Shafaii Moghadam et al., 2017). The Ashin rocks represent one of the very rare witnesses of the Neo-Tethyan suture across several thousands of kilometres (i.e. from Turkey to India). Thus, refining our understanding of the Pressure-Temperature-time (P-T-t) evolution of the rocks forming the Ashin complex is crucial. The variety of metamorphic ages and the ubiquitous disequilibrium textures (Angiboust et al., 2016; Shafaii Moghadam et al., 2017), which at a first sight represent an obstacle for fine-tuning the timing of the Cretaceous metamorphic imprint, may perhaps be viewed as an opportunity for understanding and quantifying the long-term evolution of the subduction thermal gradient and hence, yield crucial information for paleo-geographic reconstructions. Indeed, on a paleogeographic perspective, the precise configuration of both the northern and southern subduction zones that were active in the Neo-Tethyan basin located to the North of Arabia during Cretaceous is still unresolved (e.g. Alavi, 1994; Agard et al., 2007; Hassanzadeh & Wernicke, 2016; Burg, 2018; Bonnet et al., 2020). In this regard, the Ashin complex may constitute a cornerstone for deciphering this missing piece of the Zagros subduction history. We herein report the first evidence for partial melting of some of the rocks forming this paleo-accretionary complex, provide new P-T-t data and discuss the implications of these findings for the regional geodynamics and the long-term evolution of the Neo-Tethyan realm.

## 2. GEOLOGICAL SETTING

### 2.1. The Neo-Tethys Ocean

The Neo-Tethys Ocean separated Eurasia from the continents derived from Gondwana (e.g. Stampfli and Borel, 2002; Blakey, 2008). Subduction initiated in the Late Jurassic-Early Cretaceous, as recorded by several calc-alkaline volcanic arcs scattered along southern Eurasia, such as part of the Durkan volcanics in Iran in the Sanandaj-Sirjan (SaSZ) domain (Burg, 2018; Esmaeili et al., 2020). The evolution of the Northern Neo-Tethys subduction zone is mainly documented from ophiolites along the Indus-Yarlong-Tsangpo suture (e.g. Xigaze; Hébert et al., 2012). A second episode of subduction initiation occurred at 105-110 Ma (Guilmette et al. 2018), giving birth to a Southern Neo-Tethys subduction, whose ophiolitic remnants are scattered from Troodos (Cyprus) to the Spongtang ophiolite in the western Himalaya (Agard et al., 2007). The Late Cretaceous obduction of the Neiriz and Semail ophiolites North of Arabia is linked to the evolution of this Southern Neo-Tethys subduction (Agard et al., 2011).

The fabric of the Neo-Tethys Ocean commonly displays Oceanic Island Basalts (OIB), especially around 90-130 Ma (Mahoney et al., 2002; Yang and Dilek, 2015; Esmaeili et al., 2020), which testifies to an enhanced plume activity across the Neo-Tethys realm. The episode of initiation of the Southern Neo-Tethys subduction may be part of a global plate reorganization event around 105-110 Ma (Matthews et al., 2012; Rodriguez et al., 2021), well recorded by the magnetic anomalies on the Indian Ocean's seafloor (Olierook et al., 2020). A change in the dynamics of the subduction zones surrounding the Indian Ocean is invoked as a likely driver for this event, including the deactivation of a subduction segment dipping beneath the Lhasa continental terrane (Li et al., 2018). This period of global plate reorganization may correspond to a period of global slow-down in plate velocities (Olierook et al., 2020), although the seafloor magnetic record is difficult to decipher for this time span. The evolution of the segments of the Northern Neo-Tethys subduction that used to run between Eurasia and Arabia in the Cretaceous is less documented (i.e. less well-preserved) than the segments preserved in Tibet. Two suture zones (the inner Zagros and the outer Zagros belts) are observed oriented parallel to the SaSZ and correspond to various remnants of the Tethyan basin that were accreted against the SaSZ during convergence and subsequent collision between the Arabian and Eurasian plates in the Cenozoic (e.g. Agard et al., 2007; Hassanzadeh & Wernicke, 2016; Ajirlu et al., 2016 and references therein).

### 2.2. The Zagros orogeny

The Zagros orogen is a relatively young mountain belt formed by the collision between the Arabian plate and the Iranian margin over the last 30 Ma (e.g. Berberian & King, 1981; Agard et al., 2011). This collisional stage was preceded by a long-lasting NE verging subduction of the Neo-Tethyan lithosphere under the thinned Iranian margin, inferred to have initiated during middle Jurassic times (c. 180 Ma; Berberian & King, 1981; McCall, 1997; Dercourt et al., 1993). Extensive calc-alkaline arc magmatism occurred in the upper plate between Jurassic and Eocene times along the SaSZ and the Urumieh Dokhtar magmatic arc (Alavi, 1994; Kananian et al., 2014; **Fig.1A**). The SaSZ and the Urumieh Dokhtar complexes extend between the Bitlis area in Turkey down to the Makran area (Sengör et al., 1988) and were formed by a collage of various terranes against Central Iran (Hassanzadeh & Wernicke, 2016). The SaSZ comprises a variety of metamorphic rocks preceding the Arabia-collision as well as accreted fragments of the Iranian margin (Arfania & Shahriari, 2009). In the studied Hajiabad-Esfandagheh area, SaSZ rocks (locally named as Sikhoran-Sargaz Abshur complex; **Fig.1B**) comprise tectonically intercalated Mesozoic and Paleozoic high temperature gneisses, exhibiting metamorphic ages between 185 and 330 Ma (Ghasemi et al., 2002; Arvin et al., 2007). These rocks, devoid of high pressure-low temperature (HP-LT) metamorphism, were inferred to occupy an upper plate position during the oceanic subduction event (Shafaii Moghadam & Stern, 2011). The origin of the metamorphic overprint affecting SaSZ rocks is debated. In the last few years, some authors have proposed that the SaSZ magmatism and metamorphism could be related to an early Mesozoic rifting event that may have been overprinted by a Japan or Andean-type arc magmatism during mid-Jurassic times (e.g. Hassanzadeh & Wernicke, 2016; Azizi & Stern, 2019 and references therein).

### 2.3 The Hajiabad-Esfandagheh blueschists

Unlike SaSZ rocks, the Hajiabad-Esfandagheh blueschists (Sabzehei, 1974) exhibit widespread evidence for HP-LT metamorphism. These lithologies occur in a tectonic window structurally below the SaSZ Sikhoran massif in the studied area (e.g. Agard et al., 2006). They are internally formed by an antiformal stack of tectonic slices that experienced various P-T-t trajectories during their tectono-metamorphic evolution (Angiboust et al., 2016). The lowermost Siah Kuh unit, part of the "coloured mélange" as defined in literature (Delaloye & Desmons, 1980), is a pluri-kilometre sized ophiolitic massif that was weakly metamorphosed at incipient blueschist-facies conditions (c. 250 °C at 0.7 GPa) and has recently been interpreted as an almost undisturbed seamount accreted against the SW Iranian margin during the early Cenozoic (Bonnet et al., 2019). Above this lies a serpentinite-rich block-in-matrix domain (Seghin complex), mostly comprising decametre to hectometre-sized lawsonite blueschist-facies lenses of mafic tuffs associated with minor marbles (Sabzehei, 1974; Angiboust et al., 2016). Peak burial conditions, typical of a cold subduction environment (c. 450-480 °C, 1.5-1.8 GPa, 8 °C/km) were reached between 60 and 75 Ma according to multi-mineral Rb-Sr dating (Angiboust et al., 2016; see also Shafaii Moghadam et al., 2017). The shear zone separating the Seghin complex from the basal ultramafic part of the Ashin complex (**Figs.1C** and **D**) is a several hundred meter-thick serpentinized domain which comprises scarce jadeitite veins inferred to have formed at around 400-450 °C and 1.6 GPa (Angiboust et al., 2016 and references therein).

The uppermost part of the nappe-stack is occupied by the Ashin unit (Agard et al., 2006; Angiboust et al., 2016) which is internally formed from the base to the top by (i) a variably thick (0-500 m) harzburgitic to dunitic sequence (comprising chromitite pods), (ii) slivers of blue-amphibole-bearing, phengitic quartzites, (iii) a strongly folded and foliated garnet micaschists sequence with minor metabasites, marble and meta-chert intercalations and (iv) an uppermost, tens-of-meters thick association of metabasite and meta-sedimentary layers (**Figs.1C** and **D**). Agard et al. (2006) and

Angiboust et al. (2016) have reported amphibolite-facies conditions for Ashin garnet micaschists with temperatures in the order of 550 °C and pressures close to 1 GPa. The K-Ar ages published so far for Ashin micaschists are quite scattered, at c. 79 ± 2 Ma, 82 ± 1 Ma (Ghasemi et al., 2002), 98 ± 2 Ma and 101 ± 2 Ma (Delaloye & Desmons, 1980). More recently, Agard et al. (2006) reported similar in situ white mica $^{40}$Ar-$^{39}$Ar ages of 82-102 Ma and 89-109 Ma for Ashin complex garnet micaschists. Multi-mineral-based Rb-Sr isochron ages (Angiboust et al., 2016) revealed that the base of the Ashin complex (namely the quartzites) yield slightly younger (78-96 Ma) ages, interpreted as dating the end of syntectonic mineral equilibration. In contrast, the uppermost part (the garnet micaschists and the marbles) yields ages in the range of 92-101 Ma. Interestingly, an amphibolite sample collected in the uppermost part of the Ashin complex and displaying evident textural and isotopic disequilibrium features yielded a poorly constrained, but clearly older multi-mineral Rb-Sr age in the range of 110-130 Ma. Equally old ages of 124-136 Ma were also reported in Shafaii Moghadam et al. (2017) using a similar methodological approach. The significance of this large age spread recorded in Ashin complex rocks will be hereafter discussed in the perspective of a new tectono-metamorphic model.

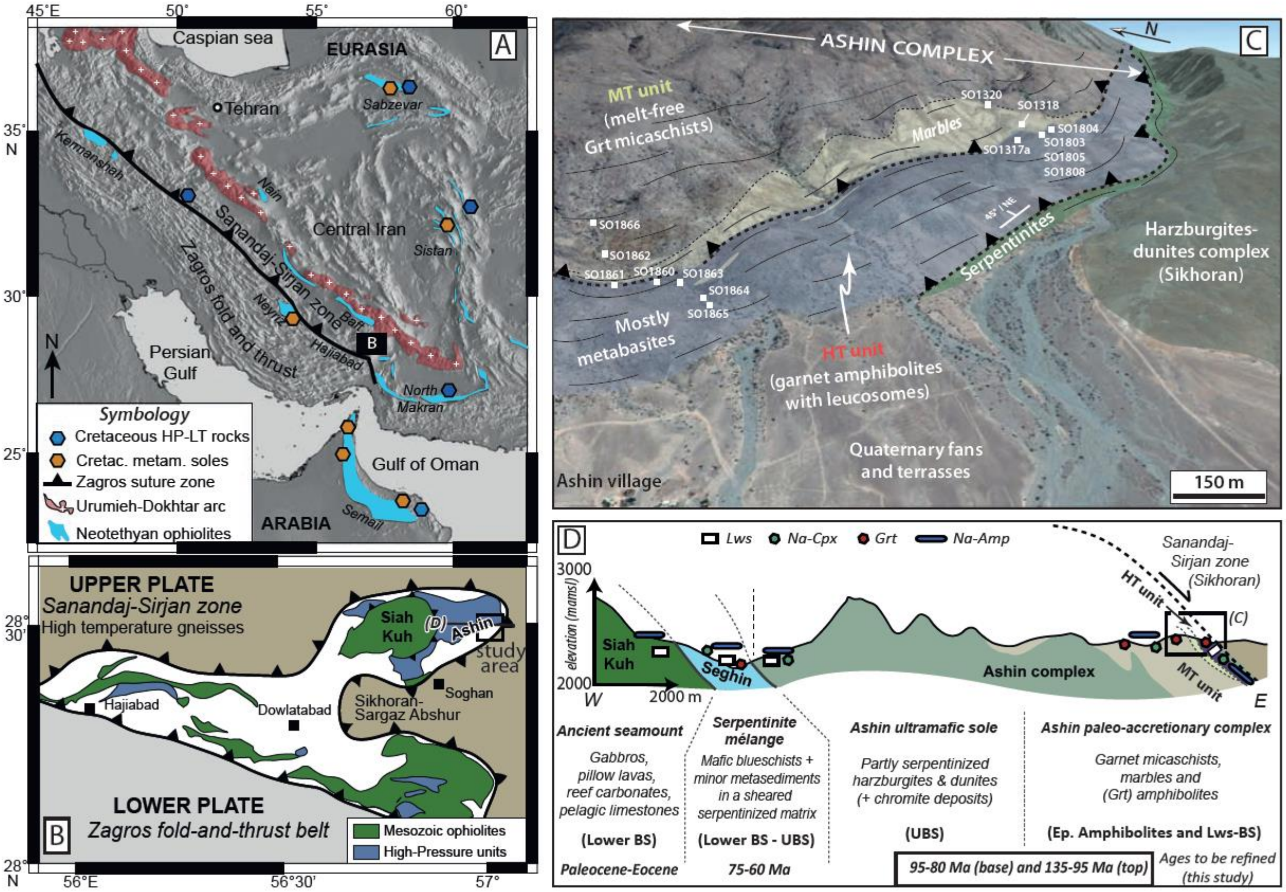

***Figure 1.*** ***A***. *Regional tectonic map locating the position of the Zagros suture zone, the ancient Urumieh Dokhtar arc as well as the main tectonic units reported in this study. The studied area is located in B. (modified after Bonnet et al., 2020).* ***B***. *Simplified geological map of the study area locating the Mesozoic ophiolites, the units affected by a HP-LT overprint and the major thrust contacts in the area (modified after Agard et al., 2006).* ***C***. *Panorama (Google Earth image) of the study area (close to the Ashin*

*village) showing the various lithologies encountered, the attitude of the foliation and the sampling locations.* ***D****. Simplified cross-section exhibiting the main relationships between the various units, the key index-minerals identified in the current and previous studies, and providing a summary of geological information for each of the units identified in this cross-section. References for ages are given in text.*

## 3. STRUCTURE AND LITHOLOGIES OF THE ASHIN COMPLEX

The upper part of the Ashin complex comprises subvertical to steeply SE-dipping slivers with distinct lithological compositions which were overthrust by the ultramafic lithologies from the Sikhoran-Sargaz-Abshur massif (SaSZ) in the study area (**Fig.1C**). The contact between these two units is lined by SE-dipping level of strongly sheared serpentinites, which are transected by a late, high-angle normal fault network (N060-striking) that contributed to a piedmont morphology now visible in the Ashin village region (e.g. Agard et al., 2006). In the studied locality, a pluri-kilometre-long metabasite sliver dominantly formed by amphibolites (and locally garnet amphibolites; **Fig.2A**) as well as meter-thick marble lenses and rare garnet micaschists layers were observed, interlayered within amphibolites of the mafic sliver (referred hereafter as the High Temperature unit: HT; see below for further thermobarometric details; **Fig.1C**). Leucocratic veins and segregates (also known in the literature as exudates; **Figs.2B** and **C**) are commonly found as (i) centimetre-sized veinlets perpendicular to the host foliation, connecting to thicker drains and (ii) vein systems parallelized to the main foliation, commonly stretched and boudinaged along the local NE-SW striking main foliation (**Figs.1C** and **2B**). The contacts between leucocratic and host material are sharp and irregular. Locally, dark rims can be observed in the host along the vein wall. Mafic layers are locally interleaved with more felsic, meta-tuffaceous lithologies characterized by a greater amount of white mica, also parallelized with the main foliation (**Fig.2D**). In the most pelitic facies (i.e. garnet micaschists), volumetrically rare leucocratic segregations (exudates) can be macroscopically observed along layers associated with large garnet porphyroblasts (**Fig.2E**). Equally large garnet crystals are observed growing within these leucocratic segregations where they locally reach one centimetre in diameter. These leucocratic segregations, associated with melanocratic domains (observed only in the HT Ashin complex), represent features typical of partial melting processes, and are therefore referred to as leucosomes and melanosomes (restites) in the following. Field evidence suggest that little volumes of melt formed within the amphibolite, likely less than c. 6 vol.% (see the geochemistry section for further justification). A thick sequence of garnet micaschists (**Fig.2F**) capped by a several meters-thick, strongly foliated marble sliver (see Agard et al., 2006 for further structural and mineralogical data on these lithologies), referred hereafter to as the Medium Temperature unit (MT), immediately underlays the HT unit. No clear evidence of former partial melting has been observed in MT garnet micaschists. The contact between the HT unit and the underlying garnet micaschists from the MT unit is marked by a diffuse shear zone, retrogressed in the greenschist-facies and challenging to localize accurately in the field (see Agard et al., 2006 for further structural data on this transect).

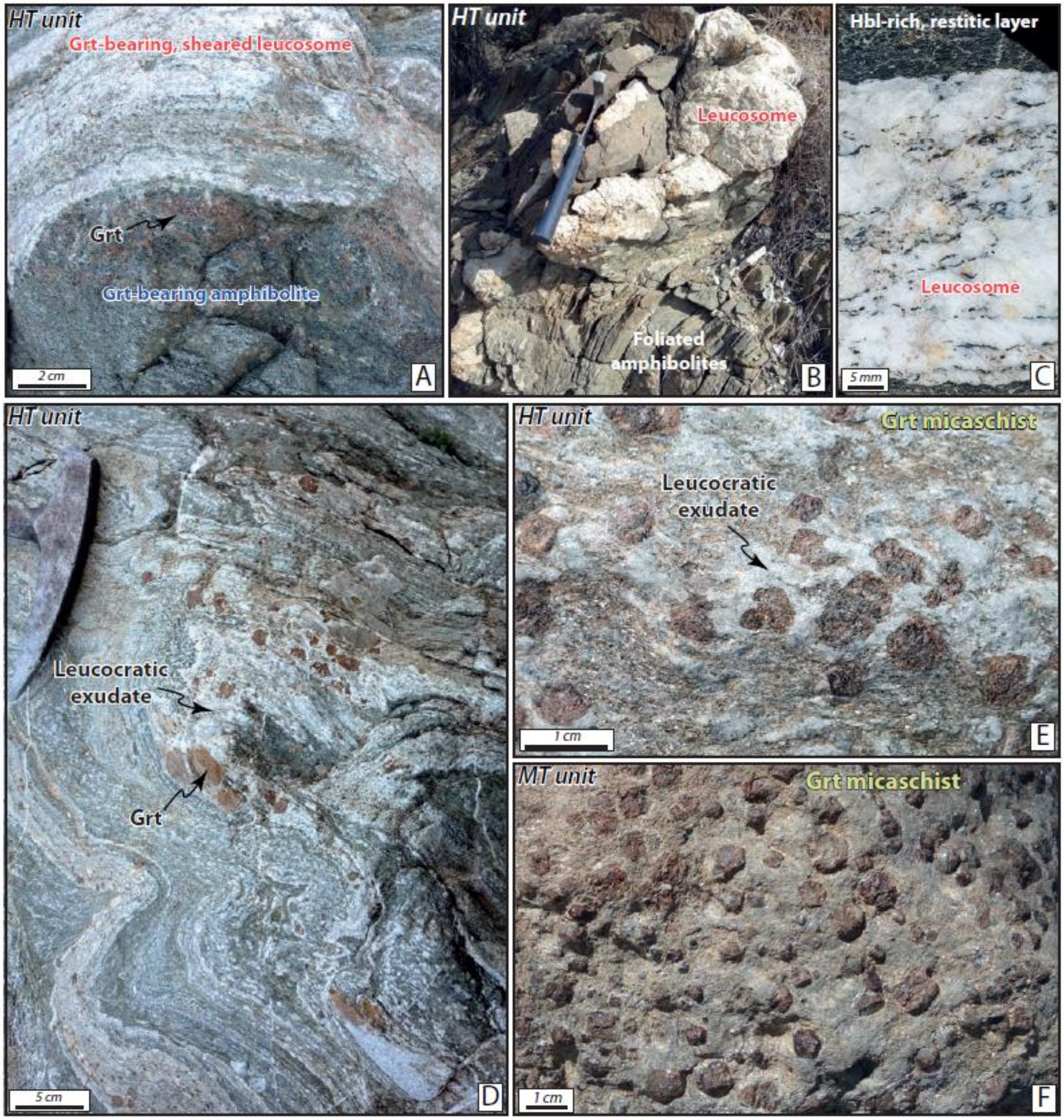

***Figure 2.*** *Field pictures of representative lithologies for HT and MT Ashin units.* ***A****. Garnet amphibolite residue with an adjacent, sheared (garnet-bearing) leucocratic domain.* ***B****. Leucocratic pocket wrapped within the amphibolite foliation.* ***C****. Close up view of a restitic hornblende-rich and associated leucocratic domains containing blueish amphibole crystals parallel to the vein walls (sample SO1317).* ***D****. Field picture of a tightly folded leucocratic domain in a mafic and tuffaceous material exhibiting centimetre -sized euhedral garnet that grew within the leucocratic band.* ***E****. Close-up view of a garnet micaschist layer displaying some leucocratic, plagioclase-rich exudates wrapping garnet along the foliation (HT unit).* ***F****. View of a representative MT unit garnet micaschist, devoid of leucocratic bands.*

## 4. ANALYTICAL METHODS

Petrographic observations, petrogeochemical and petrochronological analyses, on amphibolites, leucosome-bearing amphibolites (in both restitic and leucocratic domains) and metasediments have been performed, along with thermodynamic modelling on amphibolites. Analytical methods that were employed comprise (i) scanning electron microscope in back-scattered (SEM-BSE) mode, (ii) electron probe microanalyzer (EPMA), (iii) X-ray fluorescence (XRF) (iv) inductively coupled plasma mass spectroscopy (ICP-MS), multi-collector-inductively coupled plasma-mass spectrometer (MC-ICP-MS), in situ laser ablation-inductively coupled plasma-mass spectrometer (LA-ICP-MS) and SHRIMP measurements as well as the (v) Perple_X software (version 6.9.1).

Details of the analytical techniques, parameters and software are outlined in the supplementary material: probe measurements (section 1), whole-rock analyses (section 2), trace element laser ablation analyses (section 3), U-Pb rutile and zircon geochronology (section 4), Lu-Hf garnet geochronology (section 5), and further information regarding the choice of solid solution models for the pseudosection modelling approach (section 6).

## 5. PETROGRAPHY AND MINERAL CHEMISTRY

### 5.1 Amphibolites

The HT unit amphibolites mainly consist of medium- to coarse-grained amphibole (up to centimetric sizes, 70-80 vol%) with subordinate amounts of plagioclase, garnet, epidote, titanite, ilmenite, rutile, quartz and chlorite. These minerals define the main foliation of the metabasites. Amphiboles are euhedral to subhedral (**Figs.3A** to **C** and **E**) and correspond mostly to tschermakite and Mg-hornblende. Overall, there is no clear preferential spatial distribution in the observed variety of Mg-Ca amphibole crystals even though zones of pargasitic to edenitic compositions can be locally observed within the cores of some euhedral amphibole crystals (**Figs.4A, B** and **5A** to **D**). They exhibit blueish sodic-calcic or locally sodic as well as light green actinolitic rims (**Figs.3E, 3G, 4A, B** and **5A** to **D**). In some amphibolite samples, amphibole crystals of hornblendic composition occur as small, rounded inclusions (< 200 µm) in albitic plagioclase (e.g. **Fig.3A**). The HT amphiboles are commonly in apparent textural equilibrium with euhedral, porphyroblastic garnet or show inclusions of the latter. Within sample SO1863b, garnet (commonly chloritized along the rims and fractures) makes up to c. 5 vol% of the rock with grain diameters of commonly c. 2 mm but reaching grain sizes of up to 7 mm. Garnet is zoned, with a composition in the range $Alm_{50\text{-}70}Prp_{1\text{-}10}Grs_{20\text{-}50}Sps_{1\text{-}2}$ (**Fig.4C**). Garnet from a garnet-rich layer in sample SO1860 (hereinafter referred to as "garnet-amphibolite") exhibit atoll-like textures. Ca-Mg-Fe clinopyroxene in the range of $CEn_{33\text{-}41}CFs_{16\text{-}35}Wo_{30\text{-}49}$ (augite and diopside; **Figs.4D** and **E**) are observed as inclusions within garnet in the garnet-amphibolite (SO1860). In addition, Angiboust et al. (2016) have reported rare omphacite needles and Mg-riebeckite overgrowing prograde Ca-amphiboles in mafic lithologies from the Ashin complex. Epidote or zoisite commonly occurs as blocky grains on the rims of or within amphibole crystals and/or in association with garnet (**Figs.3B, F** and **S1A** to **D**). Epidote is observed to be locally replaced by lawsonite. Vermicular intergrowths (myrmekitic-like) of epidote associated with albite are locally observed in interstitial leucocratic domains within the amphibolite (**Fig.3F**). Titanite displays varying grain sizes (up to millimetre size values). It is mostly observed as irregular grains occurring with amphibole or within amphibole rims, and rutile and ilmenite relics can often be observed within the titanite crystals (**Figs.3H** and **5E** to **G**). In sample SO1861b, an extremely Ca-rich sample (20.49 wt.% CaO, see **Table S3**), titanite further occurs as coarse subhedral grain in association with zoisite and amphibole (**Fig.3B**). Further, albite-rich plagioclase ($Ab_{85\text{-}95}$) and quartz are commonly found within the interstitial spaces of amphibole, epidote and garnet (**Figs.3A** and **H**). In sample SO1861b, clustered and oriented clinozoisite makes up a volumetrically important domain ("zoisitite"; **Fig.3B**). Late chlorite is observed in association with titanite and replacing garnet crystals (**Figs.3A** and **H**).

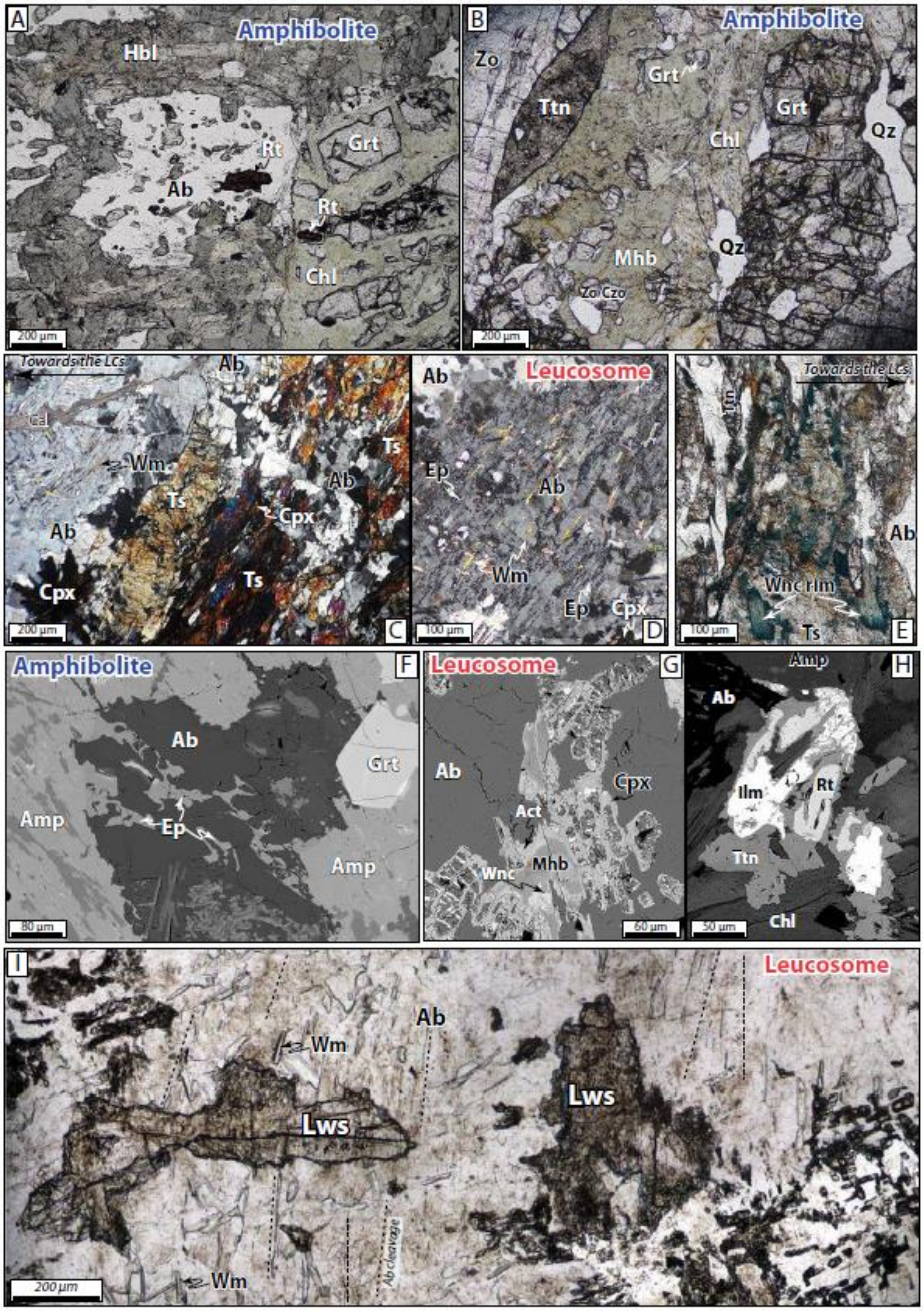

***Figure 3.*** ***A*** *to* ***E.*** *Optical polarized light photomicrographs (crossed polarizers used for Fig.3C and D) of representative amphibolites and leucosome domains from the Ashin HT unit.* ***F*** *to* ***H.*** *Backscattered electron images of amphibolite and leucosome domains highlighting relevant mineral textures (see the main text) from the Ashin HT samples.* ***I****. Optical polarized light photomicrograph of a leucosome domain from the Ashin HT unit. Note the occurrence of lawsonite crystals randomly oriented with respect to the plagioclase cleavage. Lcs. – leucosome.*

### 5.2 Leucosomes

Leucosomes from the HT unit comprise coarse-grained plagioclase + quartz and subordinate white mica + amphibole + titanite + rutile + chlorite + epidote ± clinopyroxene ± lawsonite (**Figs.3C** and **D**). The interfaces between amphibolite and the leucosome domains are generally parallel to the main foliation defined by the orientation of amphibole crystals. Both domains are spatially connected through plagioclase-filled microfractures (200 – 400 µm wide) crosscutting the amphibolite fabric (**Fig.3C**). In contrast to other mineral phases and the amphibolite matrix, plagioclase from the leucosomes displays subgrains, undulose extinction and serrated grain boundaries. Locally, garnet crystals are fractured and boudinaged within the plagioclase-rich, leucosomes matrix (e.g. **Fig.2D**). The leucosomes are chiefly made of albitic plagioclase (up to 80 vol%; $Ab_{80\text{-}99}$), although X-ray mapping and cathodoluminescence imaging revealed the presence of a clear patchy zoning pattern with oligoclase domains (**Figs.5H** and **S2**). K-feldspar has not been observed in the leucosomes. In the leucosomes, white mica occurs as 100 µm to 1 mm long laths, either as randomly oriented inclusions within coarse plagioclase crystals or as oriented crystals along the plagioclase cleavages (**Figs.3D, I** and **5H**). Dense clusters associated with epidote (**Figs.3C, D** and **G**) in "saussuritized" domains are also observed.

Muscovite cores commonly exhibit thin phengitic rims showing a clear Tschermak substitution trend with increasing Mg and Si at the expenses of Al, while Na-richer cores are locally observed (**Figs.4F, 5E, F** and **G**). Large rutile grains (which were separated for Zr-in-rutile thermometry, see below) are commonly rimmed by titanite (e.g. **Fig.5E**). Some acicular actinolite grains grow along the cleavage planes of medium-grained plagioclase crystals in sample SO1317. Single small crystals of Mg-hornblende have been identified within the leucosomes. In the leucosome-restite interface (**Figs.5A** to **D**), amphibole is strongly zoned with compositions ranging from Mg-hornblende to tschermakite (locally edenite and pargasite) in the cores and winchite to actinolite towards the rims. Some elements such as Al and Ti are particularly enriched in the cores, the latter showing an exceptionally well-defined pattern (**Fig.5C**). The calculated XMg ($Mg/(Mg+Fe^{2+})$) values are generally high (above 0.5), with higher values towards the actinolitic rims but never reaching tremolitic values (**Figs.4A** and **5D**). Epidote is commonly $Fe^{3+}$-poor (**Fig.S1**) and occurs associated with or overgrowing amphibole (e.g. **Fig.5A**). Furthermore, minor amounts of dark brown, prismatic clinopyroxene (of aegirine composition; **Fig.4D**) occur as fine-grained aggregates or fibro-radial clusters (**Figs.3C** and **G**). They seem to have nucleated on other minerals such as hornblende or a previous (now pseudomorphed) clinopyroxene (**Fig.3G**). Chlorite occurs in the interstitial space between plagioclase crystals. Interestingly, rare lawsonite crystals are observed statically overgrowing plagioclase within the leucosome or filling micro-fractures (**Figs.3I** and **5H;** see also **Table S2** for mineral chemistry data). Pumpellyite and calcite occur in the leucosomes as patches and late veins (**Fig.S2B**), respectively. The paragenetic sequence observed in amphibolites and associated leucosome domains is summarized in **Fig.6**.

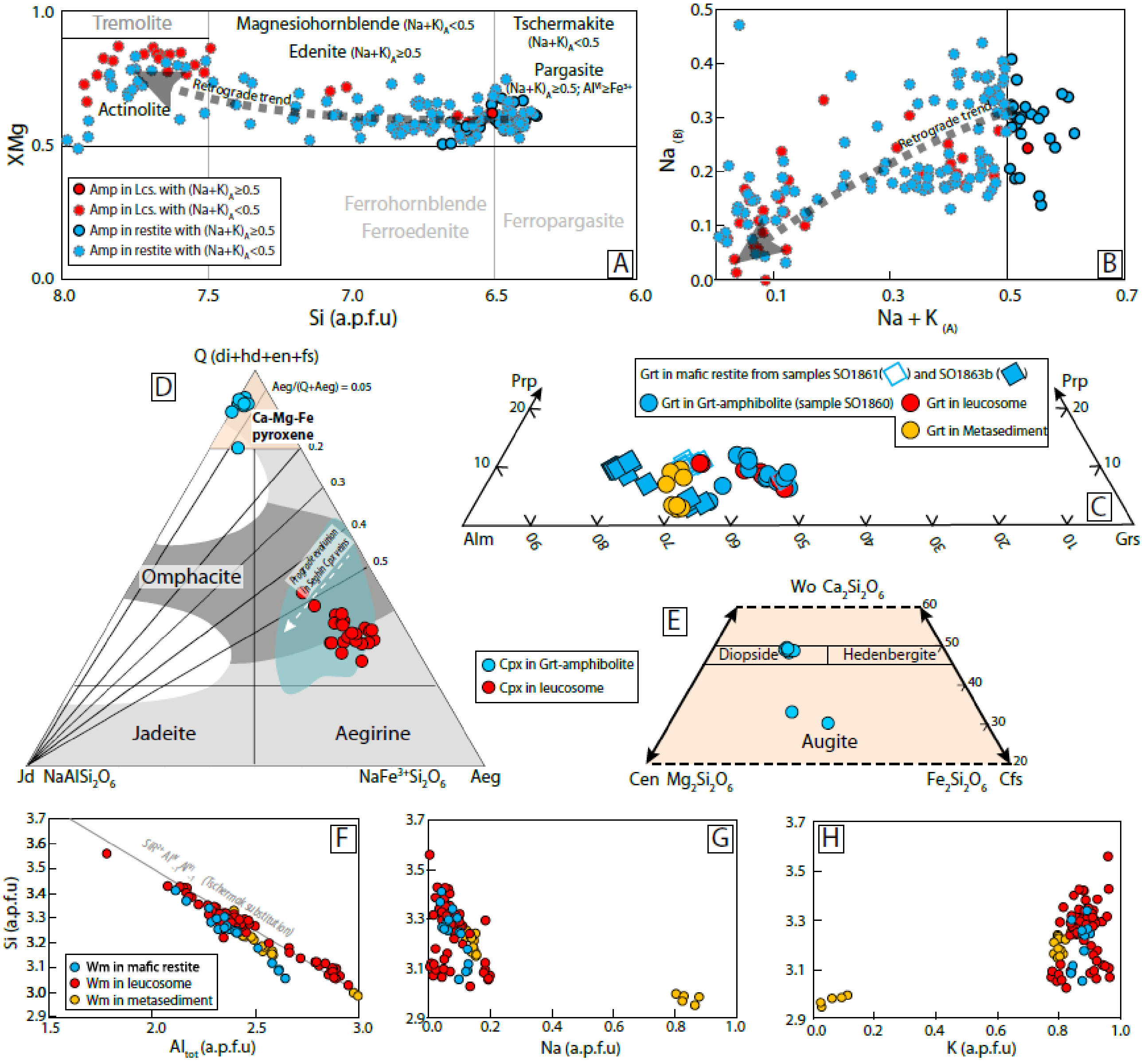

*Figure 4. Summary of mineral chemistry results of amphibole (**A** and **B**), garnet (**C**), clinopyroxene (**D** and **E**) and white mica (**F** to **H**) in samples from Ashin HT unit material. Additional epidote and white mica mineral chemistry diagrams are offered in **Figs. S1A** to **D**.*

### 5.3 Garnet micaschists

Garnet micaschists from the HT unit are observed interleaved with amphibolite and mafic tuffaceous levels (characterized by their relatively high white mica contents). Their mineral assemblages comprise garnet + white mica + quartz + albite + rutile as well as scarce amphibole crystals. Garnet micaschists from the MT unit comprise garnet + white mica + quartz + albite + rutile + ilmenite + titanite + epidote + chlorite + calcite (see **Fig.S3**). Their mineralogy as well as thermo-barometric constraints are presented in Agard et al. (2006, see also Angiboust et al., 2016 for further petrological information). Rutile occurs as oriented grains within garnet rims as well as along the main metamorphic foliation, whereas titanite forms large automorphous crystals within garnet mantles (apparently connected to the matrix via fracture networks) and rimming rutile crystals in the matrix (**Fig.S3**). Ilmenite inclusions found in garnet cores are oriented along a previous foliation. Garnet is essentially almandine with XMg contents exhibiting a slight increase towards the rims (XMg: core = 0.01, rim = 0.11, see **Fig.S3**). White mica displays three generations with phengitic cores (Si=c.3.3 apfu), muscovitic mantles (Si=c.3.1 apfu) and thin outer rims of phengitic composition (Si=c.3.4 apfu; **Fig.S3**). In addition, rare paragonite (K=c.0.03 to 0.1 apfu) has been observed within the matrix around garnet (**Figs.4G** and **H**).

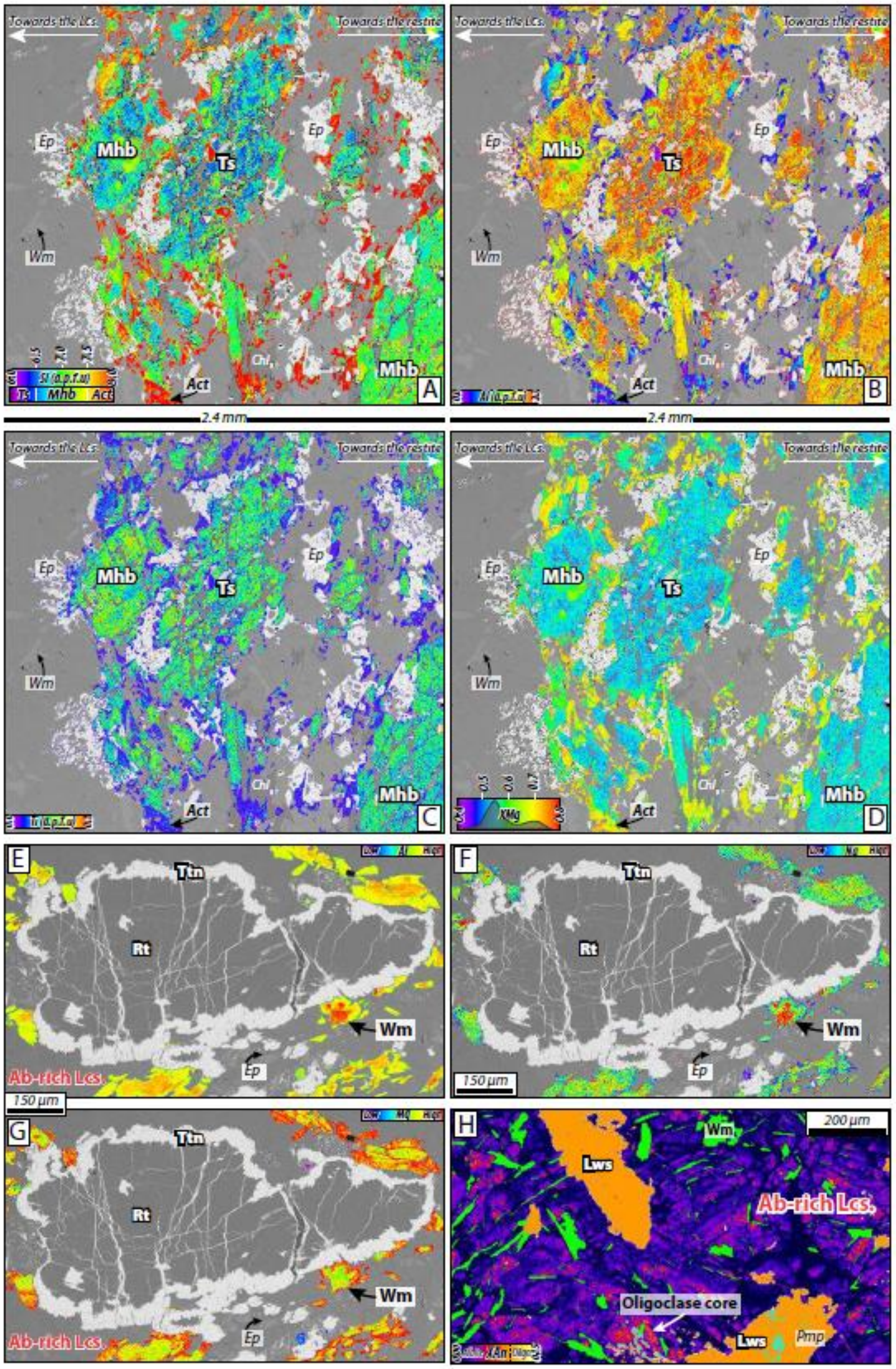

***Figure 5.*** *X-rays maps from Ashin HT unit samples highlighting multiple recrystallization and metamorphic events recorded in these rocks.* ***A*** *to* ***D****. Leucosome-restite interface emphasizing amphibole textures. Note that in panel D, the XMg ratios have been calculated assuming all iron as* $Fe^{2+}$*, thus these ratios are slightly underestimated.* ***E*** *to* ***G****. Leucosome view highlighting rutile and white mica mineral textures.* ***H****. Albite-rich leucosome depicting mineral zoning characterized by higher anorthite component towards plagioclase cores. Note the occurrence of lawsonite overgrowing the leucosome fabric.*

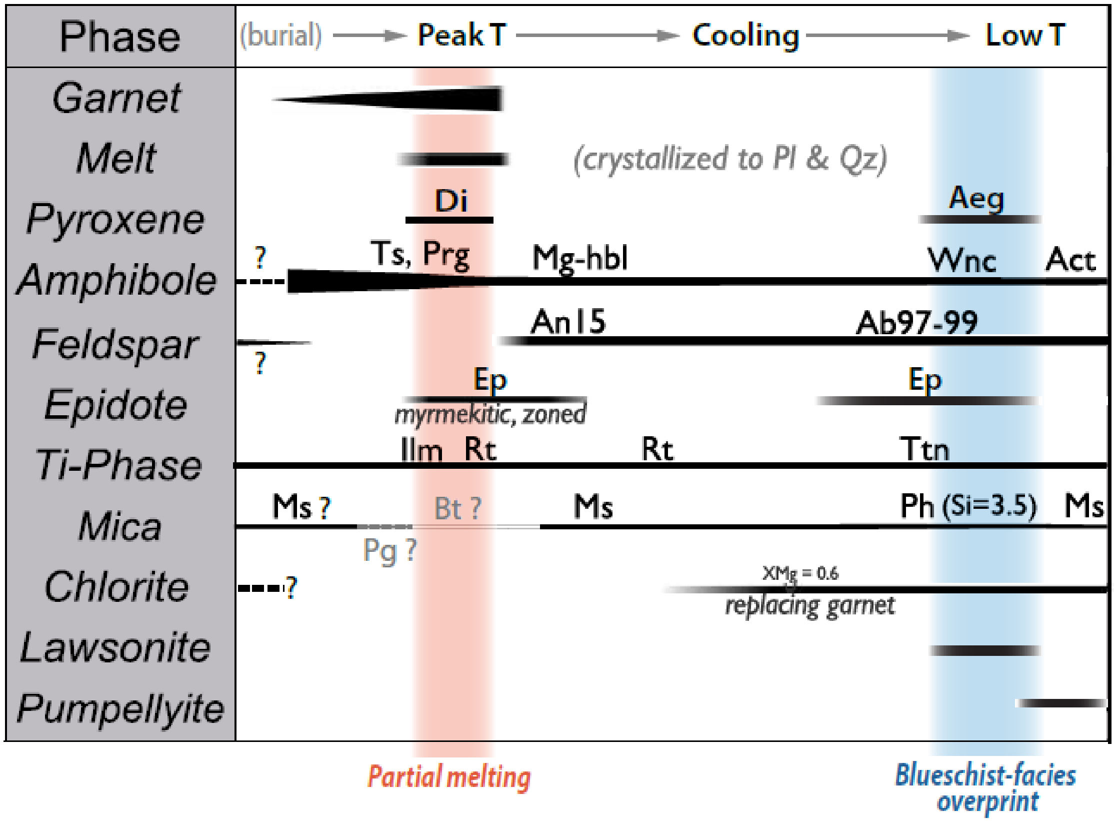

***Figure 6.*** *Occurrence table summarizing the paragenetic evolution throughout the metamorphic history recorded by Ashin HT unit samples.*

## 6. WHOLE-ROCK GEOCHEMISTRY

### 6.1 Amphibolites

Garnet amphibolite and amphibolites show major element compositions with $SiO_2$ varying between 41 and 55 wt.% and $Na_2O+K_2O$ varying between 1.7 and 7.4 wt.% (excluding the zoisite-rich sample SO1861b), belonging thus to the picro-basalts and basalts fields in a TAS diagram (up to basaltic trachy-andesite for one sample; **Table S3**). Within these samples, there is an important spread in MgO-contents between 3.5 and 11.7 wt.%. The samples mineralogically and texturally considered as restites appear relatively depleted in $SiO_2$ wt.% (cf. Table S3). The chondrite-normalized Rare Earth Elements (REEs) pattern shown in **Fig.7A** for Ashin HT unit amphibolites span a range between N-MORB and

OIB endmembers. Their Heavy Rare Earth Elements (HREEs) generally define a nearly flat pattern, whereas some amphibolites show relatively enriched Light Rare Earth Element (LREE) concentrations. The Th/Yb versus Nb/Yb diagram from Pearce (2008) (**Fig.7B**) is generally used for tracking mantle sources (Nb/Yb) and the effect of crustal components (Th/Yb), making use of two highly and nearly equally incompatible elements in mafic magmas (Th and Nb). The two elements are considered as sensitive indicators of crustal involvement due to magma-crust interaction or to inheritance of subduction components (Pearce, 2008). In this diagram, the Ashin HT unit rocks are distributed between normal N-MORB patterns (four samples) and substantially enriched signatures (five samples) showing considerably higher Th/Yb ratios than the MORB-OIB array.

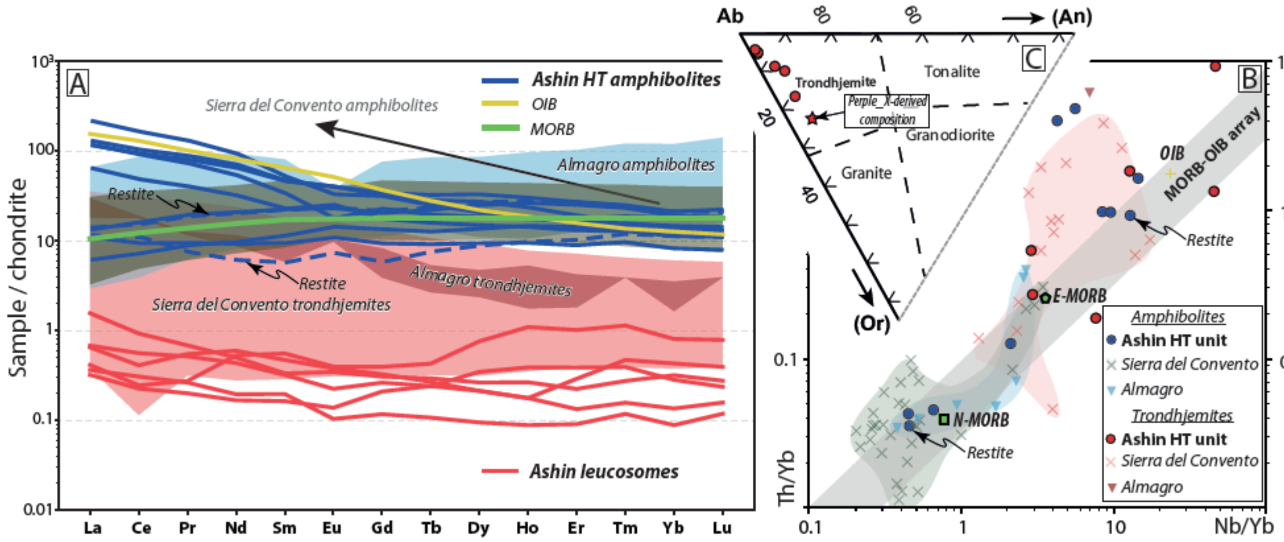

*Figure 7.* ***A.*** *Chondrite-normalized trace element patterns for the suite of studied samples including Ashin leucosomes and amphibolites. Data from other geological settings (Diego de Almagro Island, Patagonia; Angiboust et al., 2017 and Sierra del Convento-La Corea areas, Cuba; Lazaro et al., 2011; Blanco-Quintero et al., 2011) as well as OIB and MORB patterns are shown for comparison.* ***B****. Trace element Th/Yb versus Nb/Yb diagram (from Pearce, 2008). For reference, the composition of several trondhjemite samples were also plotted in this diagram originally designed for primitive basaltic rocks.* ***C****. Classification of granitoids in the An-Ab-Or normative projection (after the classification of Barker, 1979). The red star is the theoretic composition predicted at 680 °C and 1.2 GPa using thermodynamic modelling.*

### 6.2 Leucosomes

Major element data from Ashin HT leucosomes yields $SiO_2$ contents ranging between 62 and 66 wt.%, very high $Na_2O$ contents between 9 and 11 wt.% and low $K_2O$ and CaO contents (0.2-0.8 wt.% and 1.1-4.4 wt.%, respectively; **Table S3**). Iron and magnesium contents are also very low (<0.4 wt.%). These leucosomes thus belong to the trachytic field in a TAS diagram. Several of these samples correspond to the field of trondhjemites according to the classification of O'Connor (1965) and with the fields of Barker (1979) as shown in **Fig.7C**. The chondrite-normalized patterns from **Fig.7A** show considerably low REE concentrations, where the LREEs largely overlap with trondhjemitic signatures from other localities such as Isla Diego de Almagro and Sierra del Convento and La Corea, while HREEs contents are slightly lower. In the Th/Yb vs Nb/Yb diagram (**Fig.7B**), the Ashin leucosomes also overlap with those from the Sierra del Convento locality, spanning a range between average OIB and E-MORB compositions.

## 7. GARNET LU-HF DATING

The Lu and Hf concentrations, $^{176}$Lu/$^{177}$Hf and $^{176}$Hf/$^{177}$Hf ratios for the HT garnet micaschist sample SO1803a are reported in **Table S4**. Hf isotope data are reported against the JMC-475 Hf standard value of $^{176}$Hf/$^{177}$Hf = 0.282160 (Vervoort & Blichert-Toft, 1999). For age calculations, an uncertainty of 0.5% is used for $^{176}$Lu/$^{177}$Hf ratios. Uncertainties in the $^{176}$Hf/$^{177}$Hf ratios are reported as the internal precision (shown as 2 σ S.E. in **Table S4**) of the analyses, are determined by within-run statistics.

Lu and Hf concentrations in analysed garnets display consistent concentrations of ~1.8 µg/g and ~0.04 µg/g, respectively (**Table S4**). Resultant $^{176}$Lu/$^{177}$Hf ratios in garnet range from ~5.6 to ~6.1, suggestive of clean separates lacking the incorporation of deleterious Hf-rich inclusions during the full dissolution process (i.e. zircon). The tabletop-digested whole rock and matrix have significantly lower Hf concentrations than the bomb-digested whole rock and matrix (~0.1 and ~0.05 µg/g vs. ~5.1 and 3.5 µg/g, respectively), with resultant higher $^{176}$Lu/$^{177}$Hf ratios (~0.66 and ~0.77 vs. ~0.02 and ~0.01, respectively), suggesting incorporation of Hf-rich zircon during bomb digestion.

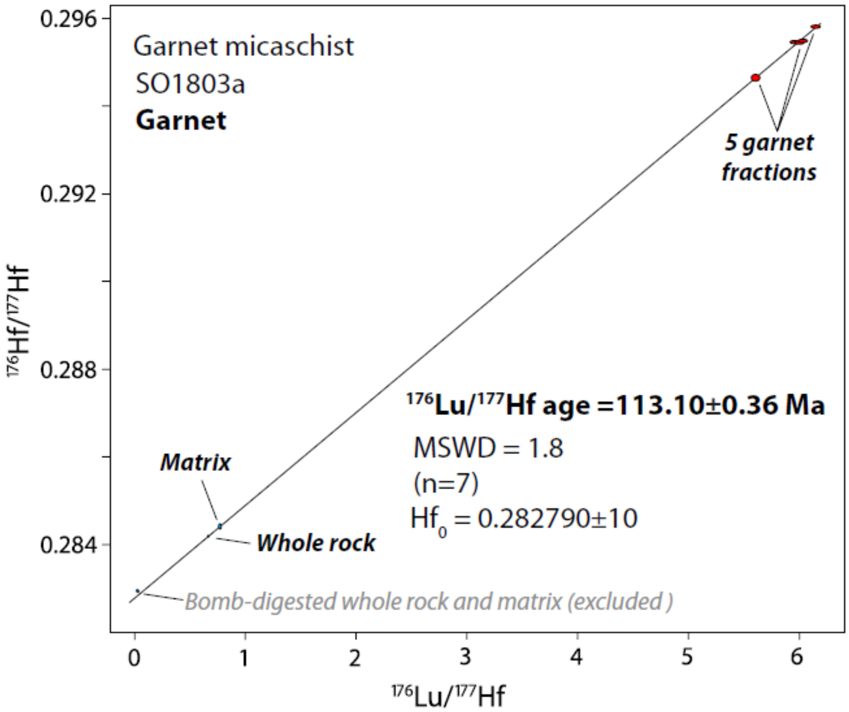

***Figure 8.*** *Lu-Hf garnet geochronology. Seven-point (five garnet fractions, tabletop-dissolved whole rock and matrix) isochron age, uncertainty, MSWD and initial Hf composition for the Ashin HT garnet micaschist. Note that the bomb-digested whole rock and matrix analyses fall off the isochron (see main text for discussion).*

The Lu-Hf garnet isochron for the Ashin HT unit micaschist is shown in **Fig.8**. The isochron age was calculated with the online version of the program IsoplotR (Vermeesch, 2018) using a $^{176}$Lu decay constant of 1.867 x $10^{-11}$ $yr^{-1}$ (Söderlund et al., 2004). A regression through five garnet fractions, the tabletop-digested whole rock and matrix, and the bomb-digested whole rock and matrix yields a relatively poor (9-point) isochron date of 111.80 ± 0.26 Ma (2σ S.E.; MSWD = 21) with an initial $^{176}$Hf/$^{177}$Hf = 0.2829036 ± 12. The high MSWD likely results from inclusion of the bomb-digested whole rock and matrix samples into the isochron age calculation. Scherer et al. (2000) noted that the influence of zircon results in erroneous Lu-Hf garnet age calculations. This is corroborated by the high measured Hf concentrations of the bomb-digested whole rock and matrix (5.1 and 3.5 µg/g, respectively). In the case provided by Scherer et al. (2001), dissolution and incorporation of inherited zircon has the effect of pulling the whole rock below the "true" isochron. Here, removing the bomb-digested whole rock and matrix, yields a more reliable (7-point) isochron date of 113.10 ± 0.36 Ma (2σ S.E.; MSWD = 1.8) with an initial $^{176}$Hf/$^{177}$Hf = 0.282790 ± 10. **Fig.8** shows that the bomb-digested whole rock and matrix lie above the 7-point, ~113 Ma isochron. This is suggestive of incorporation of relatively young zircon into solution during bomb digestion (see section 9). As such, we use the 7-point isochron age of 113.10 ± 0.36 Ma in further interpretations and discussion.

## 8. RUTILE U-Pb DATING AND ZR-IN-RUTILE TEMPERATURES

Rutile crystals were separated from two leucosomes (SO1803b and SO1808, HT unit), a garnet micaschist (SO1866) and a mafic amphibolite (SO1862) from the underlying MT unit. Rutile from samples SO1803b and SO1808 were sufficiently radiogenic to be dated (see results in **Fig.9**). Analyses from sample SO1808 are too scattered to yield a meaningful Tera-Wasserburg discordia age. Instead, assuming model common Pb compositions at 100 Ma for the upper intercept (Stacey and Kramers, 1975), the analyses likely reflect a scatter of dates between c. 112 and 85 Ma (without a significant correlation of dates with Zr concentrations; **Fig.9A**). Sample SO1803b yields a Tera-Wasserburg isochron age of 88.5 ± 2.8 Ma (2σ, n=138, MSWD = 1.9). The initial $^{207}$Pb/$^{206}$Pb value of 0.841 ± 0.01 (2σ) defined by the isochron agrees with the model common Pb composition at 92 Ma ($^{207}$Pb/$^{206}$Pb$_i$ of 0.841; Stacey and Kramers, 1975). However, high uncertainty might be linked to different rutile generations (although not distinguishable on the basis of trace element patterns), U or Pb loss, and all rutile analyses could correspond to ages scattered between c. 112 and 85 Ma **(Fig.9B)**, similar to what is deduced from sample SO1808.

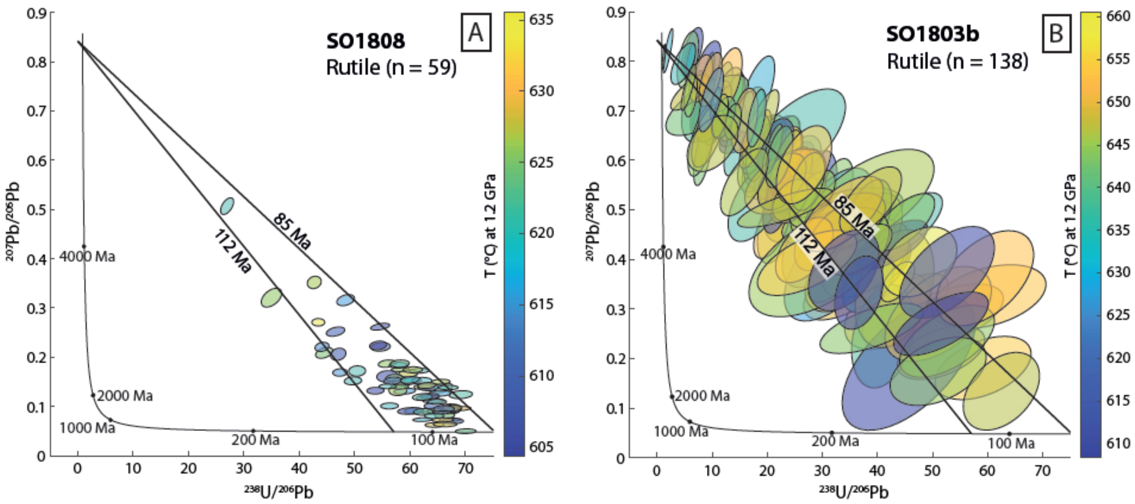

***Figure 9. A.*** *Tera-Wasserburg plot for rutile in sample SO1808, excluding analyses below 0.5 ppm of U, with the fitted discordia line. 95% confidence ellipses are color-coded for Zr-in-rutile temperatures.* ***B.*** *Tera-Wasserburg diagram for rutile crystals in sample SO1803b, with the fitted discordia line. 95% confidence ellipses are color-coded for Zr-in-rutile temperatures.*

After sorting the data by their 2σ confidence intervals, temperatures have been calculated for each rutile grain using the pressure-dependent Zr-in-rutile calibration from Tomkins et al. (2007), considered to be most precise for temperatures below 700 °C. The statistical uncertainties (2σ) are in the range of ±15-20 °C. An a priori 1.2 GPa pressure value has been chosen for the Zr-in-rutile thermometer calculations, as revealed by pressure estimates calculated in the following section, and in line with previous estimates calculated for the Ashin complex (Agard et al., 2006 and Angiboust et al., 2016). The calculated temperatures, presented in **Fig.10**, indicate that HT unit samples experienced temperatures at least in the range of 620-660 °C (c. 180-350 ppm of Zr) while sensibly cooler temperatures are derived for the MT unit (560-620 °C, c. 80-180 ppm of Zr).

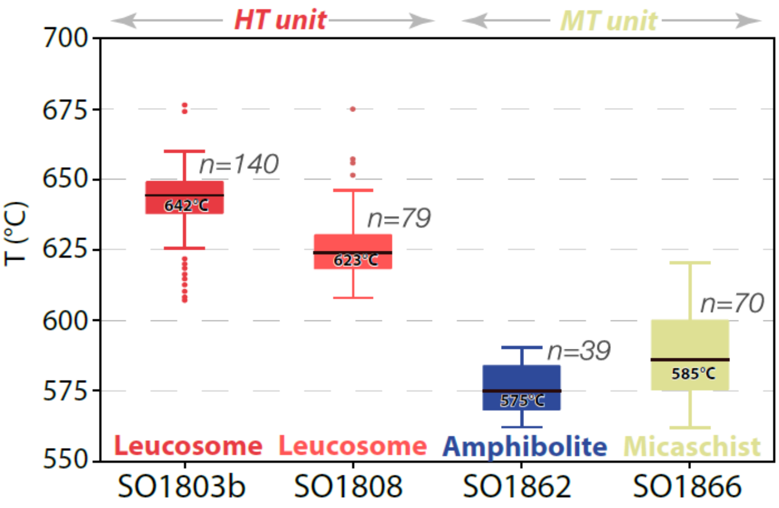

***Figure 10.*** *Zr-in-rutile results according to the Tomkins et al. (2007) calibration at 1.2 GPa for two HT unit and two MT samples.*

## 9. ZIRCON U-PB DATING, TRACE ELEMENTS AND TI-IN-ZIRCON TEMPERATURES

Sample SO1805C (a leucocratic vein) contains abundant zircon grains with several morphologies from euhedral to subhedral elongated prims with bipyramidal terminations (200 µm × 50 µm) to stubby euhedral and equant to elongated bipyramidal prisms (250 µm × 100 µm) (**Fig.11A**). Most grains are colourless and transparent, although some are pinkish translucent crystals. Cathodoluminescence imaging reveals two textural types: one population is oscillatory, patchy zoned and unzoned core grains in some cases showing metamict textures (**Fig.11A**). The second population comprises small rims, 40 µm × 20 µm, with low cathodoluminescence overgrowths partially dissolving previous group zircon grains (**Fig.11A**).

U-Th-Pb measurements on 26 different zircon cores yielded low to high concentrations of U (316–2168 ppm) and low Th (3–70 ppm) with Th/U <0.1 and little common lead (f206 ≤ 0.22%) (Table S5). All analyses are concordant (discordance −2.6 to 5.0 %) (**Fig.11B**). The weighted means (errors reported at 2σ) of the uncorrected and 207- corrected $^{206}$Pb/$^{238}$U are identical, at 104 ± 1 Ma (MSWD = 2.14) and 104 ± 1 Ma (MSWD = 1.96), respectively (**Fig.11B**). Fourteen measurements on 14 zircon rims (second population) yielded low contents of U (2-185 ppm) and very low Th (0-3 ppm) with Th/U <0.02 (**Table S5**). The rims have a high common lead component ($f^{206}$ 9-378 %), thus all analysed points are discordant (discordance 9 to 76 %) (**Fig.11C**). However, the data points define a discordia line with a lower Concordia intercept at 104 ± 3 Ma (MSWD 2.61), an age identical within uncertainty to the age of zircon cores (**Fig.11C**). A summary of available ages for the Ashin complex, including these new U-Pb zircon ages is given in **Fig.12**.

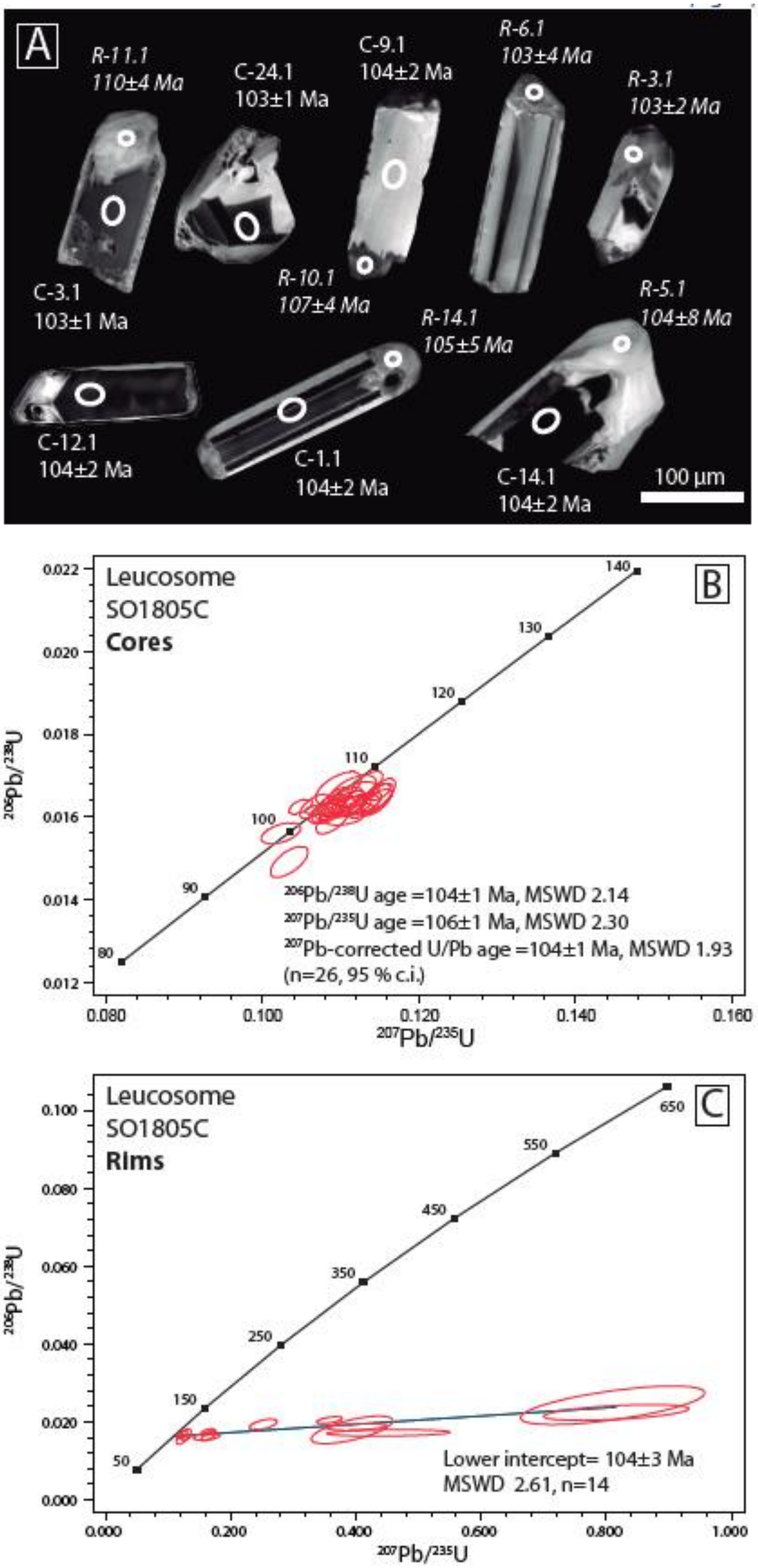

***Figure 11***. *A*. *Cathodoluminescence images and $^{206}Pb/^{238}U$ ages of representative analysed zircon*

*grains from the leucosome SO1805C. Note the core-rim texture, C and R, respectively. Wetherill concordia plots for core (**B**) and rim (**C**) populations. Cores of the analysed grains are all concordant, while rims contain large contributions of common Pb that explain discordant points.*

Trace element composition for zircon cores was obtained in the same spots of SHRIMP analysis. Due to the larger spot size of LA-ICP-MS only eight measurements were conducted on rims. The zircon trace element composition for core and rim are similar, with high REE abundances (569-6369 ppm; see **Table S5**). In the chondrite-normalized REE pattern diagram both populations have steep MREE-HREE patterns ($Lu_N/Gd_N$ = 88–3839) (**Figs.S1E** and **F**) with mainly negative Eu (Eu/Eu* = 0.06–1.02) and positive Ce (Ce/Ce* =0.75–30.03) anomalies.

For temperature estimations, we used the Ti-in-zircon thermometer of Ferry & Watson (2007). Because both quartz and rutile are found in the leucocratic veins possibly representing a part of the incipient cooling equilibrium assemblage together with zircon, their $\alpha SiO_2$ and $\alpha TiO_2$ activities were assumed to be 1 (e.g. Ferry & Watson, 2007; Li et al., 2016). Zircon cores contain 1.45 to 36.3 ppm of Ti (**Table S5**), the corresponding temperatures determined are in a range of 592-883 °C with a weighted mean of 720± 70 ºC (**Figs.13A** and **B**). Zircon rims have Ti amounts of 2–8.44 ppm (**Table S5**) and show Ti-in-zircon temperatures of 614-730 °C yielding a weighted mean of 663±40 ºC virtually identical than cores within error (**Figs.13A** and **C**).

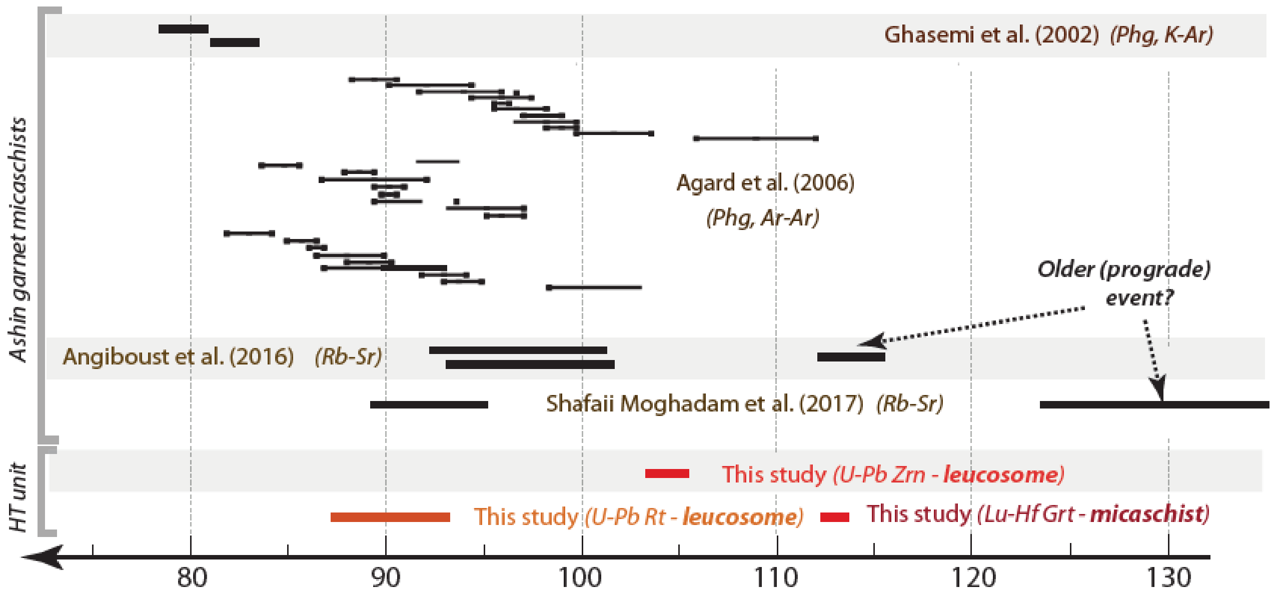

***Figure 12.*** *Summary of available geochronological constraints for upper Ashin MT and HT metamorphic rocks.*

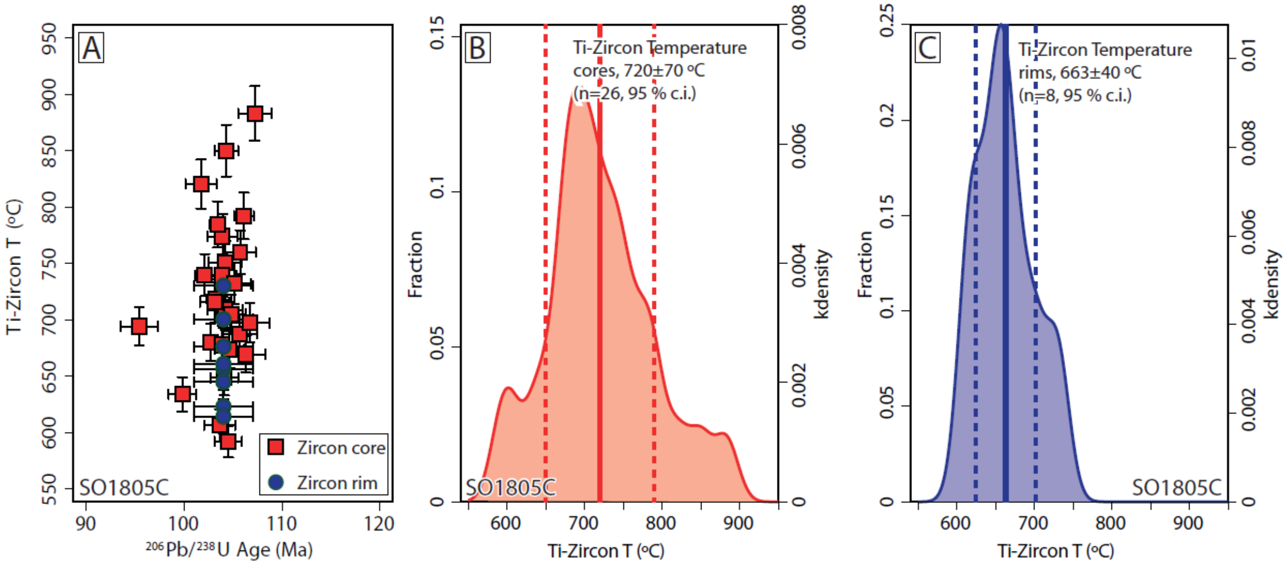

***Figure 13.*** *Ti-in-zircon temperatures from zircon crystals sampled in pelitic leucosomes (SO1805C)* ***A****. Ti-in-zircon temperatures versus crystallization ages of cores and rims.* ***B*** *and* ***C****. Distribution of Ti-in-zircon temperatures of cores and rims, respectively.*

## 10. PSEUDOSECTION MODELLING OF PARTIAL MELTING

The T-X($H_2O$) and P-T pseudosection calculations were performed using the Perple_X software version 6.9.1 (Connolly, 2005). The selected chemical system ($Na_2O$-CaO-$K_2O$-FeO-MgO-MnO-$Al_2O_3$-$SiO_2$-$TiO_2$-$H_2O$) reflects a representative amphibolite (sample SO1804B, see **Table S3**) which shows a bulk major (and trace) elements composition similar to a MORB and appears devoid of melt extraction microstructures (see section 6). It thus represents the composition inferred to be as close as possible to the mafic protolith. In sake of simplifying this chemically complex system, iron is considered as ferrous (this assumption is largely supported by the clinozoisite-rich nature of epidote observed in garnet amphibolites). This modelling approach is particularly challenging since neither mafic restite nor leucosome compositions alone properly represent the bulk composition of the system at the melt-producing conditions. The list of solid solution models used for the modelling is given in the Supplementary material.

First, temperature-X$H_2O$ pseudosections for amphibolites (500-750 °C vs 0-5 wt.% $H_2O$; **Fig.14A**) were plotted at different pressures (1.1, 1.2 and 1.3 GPa) and compositional transects were examined at 620, 650 and 680 °C in order to determine a pressure range with melt appearance consistent with further temperature estimates and mineral assemblages (e.g. best fit field in **Fig.14A** limited by the zo-out and melt-in curves). This approach is motivated by the calculated range of Zr-in-rutile and Ti-in-zircon temperatures (on samples belonging to the HT unit) which span an approximate range near 620 to 720 °C (see sections 8 and 9). Pseudosection modelling and phase abundance transects as a function of $H_2O$ contents (**Figs.14A** and **B)**, indicates that the best fit field between observed parageneses, mineral modes and modelled phase relationships is obtained for the 1.5-2.9 wt.% $H_2O$ range at 680 °C and 1.2 GPa. A complementary transect at 650 °C and 1.2 GPa also gives a very similar $H_2O$ range (**Fig.S4**), which is also in good agreement with the observed paragenesis. For this range, between 0 and 10 vol.% melt is predicted, in line with field-based leucosome volumetric amount estimates (<10 vol%). Further, 70 vol.% of a hornblendic amphibole is expected, in agreement with textures and mineral chemistry (**Fig.5**). A median value of 2.2 wt.% $H_2O$ has thus been selected to calculate a P-T pseudosection in the 1.0-1.3 GPa and 500-750 °C window (**Fig.14C**).

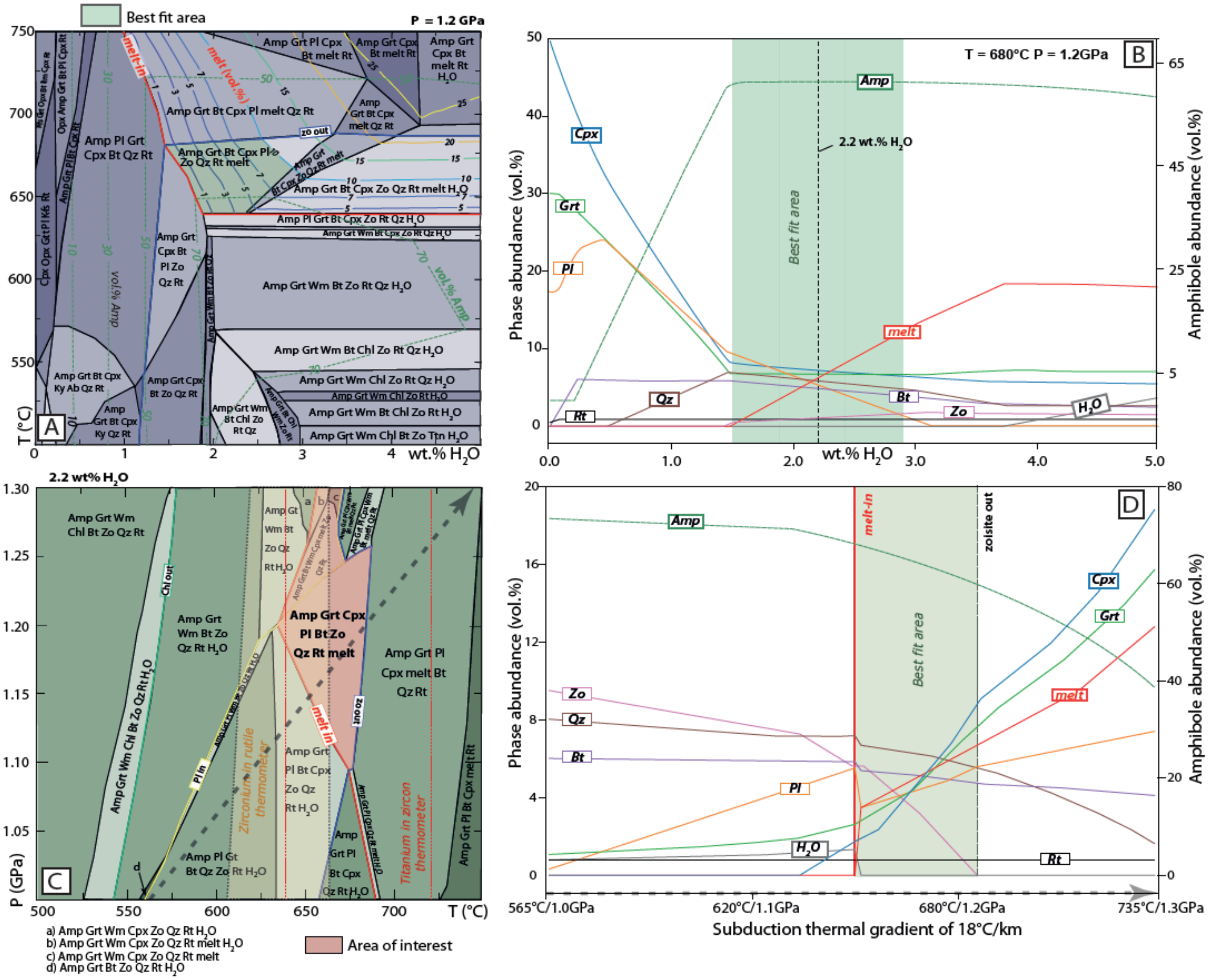

*Figure 14. Thermodynamic modelling results on sample SO1804B.* ***A****. T-X($H_2O$) pseudosection showing fields, melt and amphibole volumetric abundances as well as the region that fits better petrological observations and measurements.* ***B****. Phase abundances relative to $H_2O$ variations at fixed P-T conditions (1.2 GPa and 680 °C). Highlighted in green is the best-fit range (see text for further details).* ***C****. P-T pseudosection calculated with a fixed 2.2 wt.% $H_2O$ amount. Highlighted in red the best-fit conditions as deduced from field and sample observations. The range of temperatures calculated for sample SO1803b using the Zr-in-rutile thermometry (calibration from Tomkins et al. (2007) and for sample SO1805C using Ti-in-zircon thermometry (calibration from Ferry & Watson, 2007) are shown for comparison. The dotted line marks the P-T trajectory followed by a sample buried along a 20 °C/km thermal gradient.* ***D****. Phase abundances calculated along the prograde thermal gradient displayed in panel C. Best-fit conditions (see details of the approach in text) are highlighted with a green transparent band.*

From this model, we conclude that the best-fit region (in red) is expected for the field Amp-Grt-Cpx-Pl-Bt-Zo-Qz-Rt-melt, above the melt-in curve and below the zo-out reaction curve, in agreement with the presence of zoisite in the studied samples; **Figs.3, 6** and **S1**). The red field in **Fig.14C** largely overlaps with the Zr-in-rutile and Ti-in-zircon temperatures calculated above. The changes in the paragenetic sequence along a hypothetical prograde burial path of c. 18 °C/km (assuming a linear temperature increase up to peak conditions; see dotted lines on **Fig.14C**) is depicted in **Fig.14D**. There, it appears that the peritectic reactions in this field involve the consumption of amphibole, plagioclase and zoisite and the associated formation of garnet, clinopyroxene and melt (in agreement with processes already documented by Vielzeuf & Schmidt, 2001 for a MORB system in laboratory experiments). Note that the main discrepancy of the model with natural observations is the prediction of biotite (approximately 6 vol.% at best-fit conditions) while it has not been observed in the set of samples selected for this study. The model also does not predict ilmenite while it is commonly observed associated with rutile in the studied samples. All garnet isopleths are nearly vertical and therefore not helpful for constraining the pressure within the red field accurately. From these pseudosection investigations together with independent zircon and rutile thermometry, it is obtained that the likely peak burial P-T conditions reached by the HT unit mafic lithologies are in the range between c. 650 and 680 °C and 1.1 to 1.3 GPa (considering the uncertainties inherent with this modelling approach).

## 11. DISCUSSION

### 11.1 Partial melting in the Zagros paleo-accretionary wedge

Our field and petrographic investigations have revealed that the internal structure of the Ashin complex is less homogeneous than initially described by Agard et al. (2006) and Angiboust et al. (2016). Indeed, a several tens of meters' thick sliver occupying the uppermost structural position (the HT unit), just under the non-subducted SaSZ-derived Sikhoran complex (**Figs.1B** and **C**), exhibits clear evidence for partial melting of mafic, intermediate and metapelitic lithologies (**Fig.2**). While sub-solidus peak temperatures in the range of 500-600 °C were proposed in the immediately underlying MT unit made of garnet micaschists (Agard et al., 2006; Angiboust et al., 2016), the identification of leucosomes in mafic and pelitic lithologies reveals warmer conditions prevailing in the HT unit during peak metamorphic conditions.

The amount of Zr in rutile is considered to reflect peak metamorphic contents and conditions (Zack et al., 2004; Kohn, 2020) as rutile equilibrates its Zr content during prograde metamorphism (e.g. Penniston-Dorland et al., 2018), but seems to act as a relatively closed system during retrograde cooling (Ewing et al., 2013). Zr-in-rutile thermometry yielded temperature estimates beyond the MORB wet solidus, i.e. above 650 °C (**Fig.10**). On the other hand, pressures deduced from pseudosection modelling suggest that peak burial conditions of 1.1-1.3 GPa were attained during peak T conditions, in line with the absence of an omphacitic clinopyroxene in the peritectic assemblage which would signify pressures greater than 1.5 GPa according to Vielzeuf & Schmidt (2001; **Fig.14C**). Furthermore, at estimated peak conditions (e.g. 680 °C and 1.2 GPa), the theoretical melt composition is trondhjemitic, in agreement with analysed leucosome samples (**Fig.7C**). A discrepancy between our observations and the modelling results is the absence of biotite in our samples, while 6 wt.% is predicted using a MORB composition with 2.2 wt.% $H_2O$. While (rare) biotite inclusions in garnet from the Ashin complex have been reported by Agard et al. (2006), this discrepancy within our samples can be explained (i) by the use of a starting model composition with $K_2O$ contents greater than in the average MORB composition, and (ii) the full destabilization of all the biotite crystals presents in the system during retrograde overprinting. This latter hypothesis could be supported if considering the occurrence of chlorite as a product of biotite breakdown. Although these rocks were extensively overprinted during subsequent metamorphic re-equilibration (**Fig.5**), it is possible to determine, using pseudosection modelling and Ti-in-zircon temperatures, that supra-solidus temperature conditions nearing 680 °C were reached in this HT sliver (**Fig.14C**), in line with the experimental data from Vielzeuf & Schmidt (2001; **Fig.15A)**.

Vestiges of subduction-related melting of oceanic crust are rare on Earth (e.g. Catalina Schists: Sorensen and Barton, 1987; Cuba: Blanco-Quintero et al., 2011; Iran: Rossetti et al., 2010; Chilean Patagonia: Angiboust et al., 2017). The relatively enriched pattern in LREE as well as departure from the MORB fields towards OIB and higher Th/Yb ratios for some of the amphibolites (**Fig.7B**), may indicate (i) a contribution from a sedimentary source in the mafic protolith (as expected for instance in tuffaceous lithologies), (ii) a metasomatic overprint of the N-MORB protolith by sediment-derived fluids during metamorphism and/or (iii) slight modification of the pristine MORB signature due to melt extraction. Evidence for local melting of mafic MORB-related protolith, as expected for a paleo-accretionary environment, is supported by low Zr, HFSE and REE concentrations and the presence of trondhjemite-like signatures in the leucosomes (**Figs.7A** to **C** and **Table S3**; see also Rapp et al., 1991; Lazaro et al., 2011; Blanco-Quintero et al., 2011; Angiboust et al., 2017). The relatively flat HREE pattern (**Fig.7A)** suggests that the REE pattern of the mafic lithologies has been only weakly modified by melt extraction processes. Such elements are potentially partitioned into garnet, rutile and epidote; the stable phases during melting. The high concentration of hornblende crystals in some parts of the HT unit amphibolites and garnet amphibolites (**Figs. 2A** and **C**) confirms the restitic nature of partially molten material and indicates melt loss during the peak T event (process also visible in the residual geochemical signature of some mafic samples; **Table S3**; **Fig.7A**). On the one hand, microscopical evidence from the mafic lithologies suggests an amphibole dehydration-induced partial melting as described in the literature (e.g. Vielzeuf & Schmidt, 2001; Moyen & Stevens, 2006). Myrmekitic-like intergrowths of epidote with plagioclase indicate that epidote crystallized from a melt phase, in line with Vielzeuf and Schmidt (2001). On the other hand, the formation of a garnet-amphibole-bearing residue in some samples as associated with the observation of leucosome patches, melt channels and veinlets of melt segregations may suggest that local partial melting occurred before dehydration of prograde amphibolite (**Fig.2A**; e.g. Drummond & Defant, 1990). An external aqueous fluid source during melting is also probably required to explain the relatively high amount of $H_2O$ inferred in our pseudosection modelling approach to fit the observed parageneses (1.5-2.9 wt.%; **Fig.14**). Such $H_2O$-rich external fluids, also expected to explain the formation of Na-rich melts such as trondhjemite as well as albitites, were likely derived from prograde dehydration reactions in the underlying oceanic lithosphere. These $H_2O$-rich conditions required for melting are also supported by the occurrence of only few crystals of clinopyroxene in the amphibolites, a phase that is systematically inhibited during melting at $H_2O$-rich and high-pressure conditions (e.g. Garcia-Casco et al., 2008).

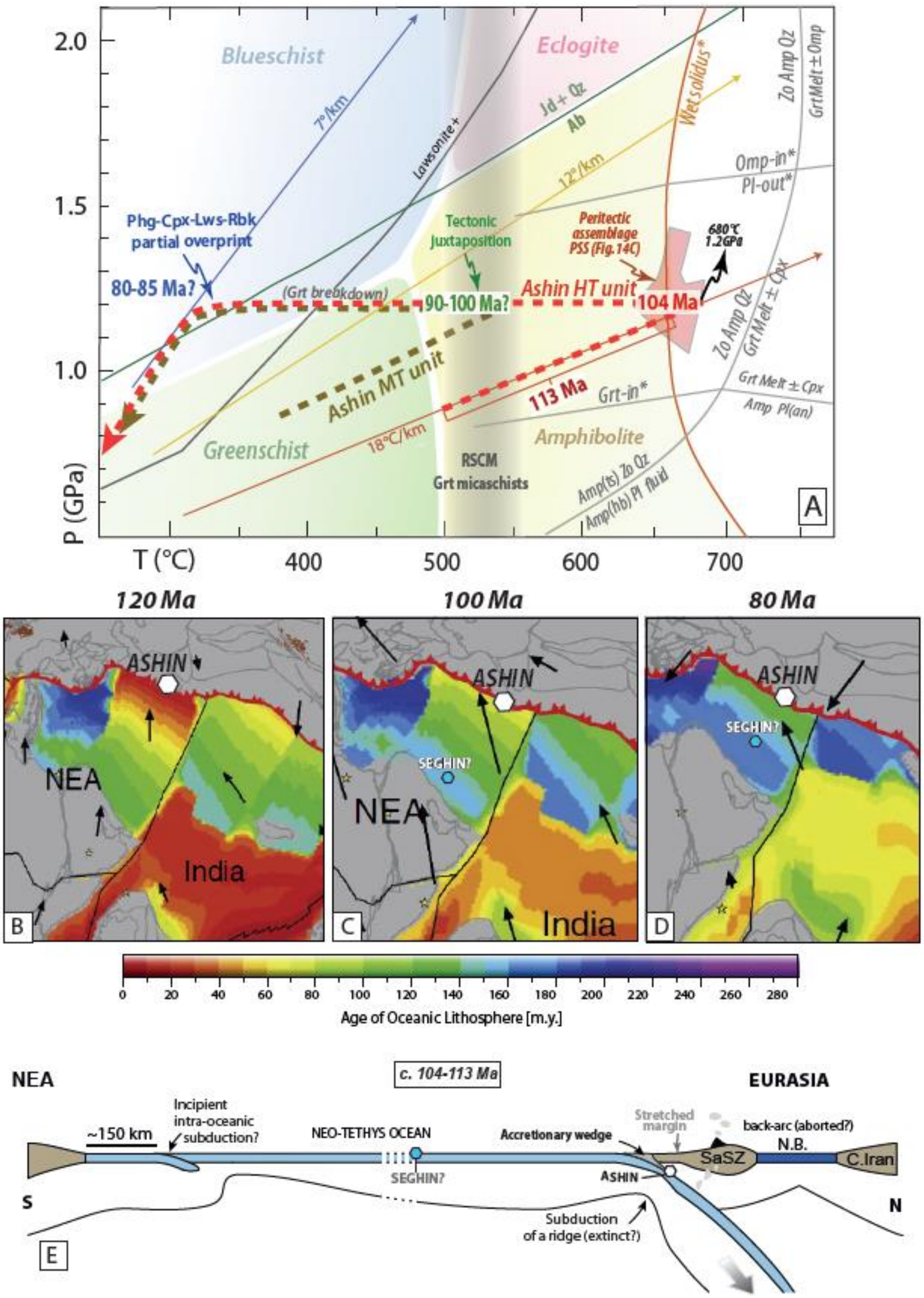

***Figure 15. A***. *P-T diagram summarizing available thermobarometric and geochronological data for Ashin HT and MT units (RSCM: Raman Spectroscopy of Carbonaceous Matter; see data in Agard et al., 2006 and Angiboust et al., 2016). Grey-coloured reaction lines and reactions marked with an asterisk symbol are derived from the experiments from Vielzeuf & Schmidt (2001) on MORB material. We explain the difference in peak burial temperatures and the spread of ages in the upper Ashin complex by the*

*tectonic juxtaposition of two distinct units that occurred likely around 90-100 Ma through underplating processes occurring at c.40km depth, i.e. towards the base of the basal accretion region of a paleo-accretionary wedge.* ***B*** *to* ***D****: Paleogeographic reconstruction of the geodynamic evolution of the Tethyan ocean between 120 and 80 Ma, revealing a ridge subduction event as well as the subduction of gradually cooler oceanic lithosphere under the Iranian margin. Absolute plate velocity vectors are denoted as black arrows (modified after Seton et al., 2012). NEA – Northeast African plate.* ***E****: Schematic geodynamic cross-section across the Tethyan realm showing the location of Ashin complex rocks, the Northern Tethyan subduction accretionary wedge and the inferred "extinct" ridge subducted under the SaSZ at c. 105 Ma (modified after Bonnet et al., 2020 and Burg, 2018).*

The timing of prograde metamorphism – at least during amphibolite-facies at pre-melting conditions (see below) – has been illuminated through Lu-Hf dating of garnet within a metasediment from the HT unit. While the age of the peak T melting event has been possible to elucidate through dating of zircon crystals (inferred to have formed during melt crystallization) from a leucocratic vein (**Fig.2B**). Garnet dating yields an age of 113.10 ± 0.36 Ma, sensibly older than the leucosome crystallization age in the range c. 104-105 Ma calculated for zircon cores and rims (**Fig.12**). We note that zircon trace element patterns, particularly HREEs, depict strong positive anomalies (**Figs.S1E** and **F**), compatible with zircon crystallization in the absence of garnet from the leucosome, a mineral with strong affinities for HREEs (e.g. Rubatto, 2002). Thus, the older garnet ages relative to zircon as well as HREEs patterns, allow us to conclude that leucosome zircon crystallized from a melt in the absence of garnet, the latter dating prograde metamorphism prior to peak T conditions. Within zircon, similar ages and trace element patterns as well as Ti-in-zircon temperatures (**Figs.S1E, F** and **13A** to **C**) among cores and rims, suggest different stages of dissolution/precipitation, probably related to variable influx of melt during the partial melting process. Note that zircon ages are older than most of the ages obtained on the underlying marbles and garnet micaschists (78-101 Ma; Ghasemi et al., 2002; Agard et al., 2006; Angiboust et al., 2016). Rutile U-Pb dates span a range (85-112 Ma) which partly overlaps the age obtained using zircon U-Pb dating (**Figs.9A** and **B**). We note that in both analysed samples from the HT unit, most grains are ~100 μm large, which according to experimental investigations might correspond to closure temperatures of the U-Pb system of ~650 °C (with a 10 °C/Ma cooling rate, Cherniak, 2000 and references therein). Consequently, this spread in the dates may reflect partial isotopic re-equilibration of peak T rutile crystals during incipient cooling in the T range 550-650 °C, as determined for the same rutile crystals using Zr-in-rutile thermometry (**Fig.10**). These observations support the inferred peak T conditions in the range of 650 to 680 °C, which are slightly hotter than the maximum temperatures estimated from Zr-in-rutile thermometry but well within the values obtained using the Ti-in-zircon thermometer.

Field relationships also suggest that this melting stage occurred in a host already exhibiting a structural fabric, thus implying a tectono-metamorphic history prior to partial melting, which is extremely challenging to decipher due to extensive recrystallization as a consequence of the protracted metamorphism. The existence of pre-113 Ma subduction activity and the formation of an associated paleo-accretionary wedge is inferred from (i) the presence of probable arc magmatism culminating at c.170 Ma all along the SaSZ (e.g. Hassanzadeh & Wernicke, 2016 and references therein) and (ii) the finding of relatively old Rb-Sr multi-mineral ages in the range 110-130 Ma (with large uncertainty due to mineral isotopic disequilibrium) in the uppermost part of the Ashin complex further to the SW (Sokhan region; Angiboust et al., 2016; Shafaii Moghadam et al., 2017), which are here interpreted as non-equilibrated domains of this paleo-accretionary system. The report of eclogites in the SaSZ in the North Shahrekord region (Davoudian et al., 2016) dated at 170-185 Ma using $^{40}$Ar-$^{39}$Ar on phengite also supports the idea of a subduction margin already active earlier during the Mesozoic. The value of the metamorphic gradient before 105 Ma remains unknown.

### 11.2 A record of the secular cooling of the Zagros paleo-accretionary wedge

The HT Ashin locality is one of the very few places worldwide where lawsonite is observed replacing mineral phases originally crystallized in an anatectic leucosome. For instance, in Sierra del Convento and La Corea regions (Cuba), blocks of mafic rocks now exposed in a serpentinite mélange have experienced partial melting followed by isobaric cooling (at 1.5 GPa) down to lawsonite blueschist-facies over a c.15-Ma time period (e.g. Garcia-Casco, 2007; Blanco-Quintero et al., 2011). The assemblage herein reported also points to a similar cooling history, as blue amphibole, lawsonite, titanite and high-Si phengite are observed, statically overgrowing the previous HT assemblage (**Figs.3, 4** and **15A**). In addition, the occurrence of paragonite-rich cores in white micas from the leucosomes (**Fig.5F**), and paragonite-rich rims around white micas (**Fig.S3**) in the garnet micaschists (**Fig.4F**), could represent a relic prograde and retrograde assemblage, respectively. Garcia-Casco (2007) estimated that the crystallization of paragonite in peraluminous melts occurs at pressures above 0.8 GPa. Thus, the finding of paragonitic white mica could support high-pressure conditions for both metamorphic events. Even though the pressure cannot be precisely constrained for the HP-LT overprint, the reported paragenesis points to lower lawsonite-blueschist-facies conditions, i.e. P-T conditions approaching 300 °C and pressures less than 1.2 GPa, based on phase relationships and mineral stability (e.g. Bonnet et al., 2019 and references therein). Field relationships and microtextures point to a relatively pervasive fluid flow that accompanied this low-T event within slices but also along the retrograde shear zones that crosscut the sequence. The presence of at least four metamorphic events in Ashin HT unit metabasites and metasediments (including a very minor, exhumation-related overprint; **Fig.6**) therefore caused extensive mineral textural disequilibrium with fluid-assisted dissolution-reprecipitation processes accompanied by isotopic disequilibria. This may explain (i) the spread in rutile U-Pb ages and (ii) the difficulty of obtaining well-constrained isochrons with the multi-mineral Rb-Sr method for phengite-bearing lithologies. Even though similar cooling-related parageneses and fabrics have been observed and reported in the immediately underlying Ashin MT unit (e.g. the garnet micaschists on **Fig.1C**), we emphasize that no clear evidence for partial melting is observed in these rocks, which according to previous Raman thermometry estimates, did not reach temperatures greater than 550 °C (Agard et al., 2006; Angiboust et al., 2016). We note that pressure estimates (0.9-1.2 GPa) for the garnet micaschist from the underlying MT unit (Agard et al., 2006) are not drastically different from those estimated for the overlying HT unit (**Fig.15A**). Geochronological studies on these rocks have not yielded ages older than those obtained for the melt-bearing sliver (see references above). From these observations, it may be speculated that (i) two slivers with distinct peak burial P-T-t conditions coexist in the upper part of the Ashin complex, (ii) they were juxtaposed after the melting within the trondhjemite-bearing HT sliver, likely around 95 Ma (according to Rb-Sr ages for the marble-bearing mylonites lining the shear zone at the base of the HT sliver; **Fig.1C**; Angiboust et al., 2016) and (iii) they underwent cooling together down to lawsonite blueschist-facies until the end of the Cretaceous (**Fig.15A**).

The record of long-term cooling in paleo-accretionary material is a rather rare event, known for instance in the circum-Pacific sutures (Franciscan: Grove & Bebout, 1995; Anczkiewicz et al., 2004; Chilean Patagonia: Angiboust et al., 2018) as well as in the Caribbean (Dominican Republic: Krebs et al., 2008; Cuba: Blanco-Quintero et al., 2011). This model implies a long-term cooling of the northern Zagros subduction thermal gradient (at least in the Ashin area) from c.18 °C/km down to c.7 °C/km within a c. 40-Ma time window (**Fig.15A**), confirming preliminary observations reported by Angiboust et al. (2016) on the Soghan region. Corresponding cooling rates range between 8 and 10 °C/Ma (considering uncertainties on the age at which the 7 °C/km gradient has been achieved), in line with cooling rate estimates obtained by previous studies on other localities (e.g. Anczkiewicz et al., 2004; Krebs et al., 2008). Higher cooling rates of c. 25 °C/Ma were proposed for the isobaric cooling event in Cuba (e.g. Blanco-Quintero et al., 2011).

### 11.3 Implications for Northern Tethyan margin geodynamic evolution

Our understanding of the geodynamic history along the northern active margin of the Tethyan realm during the Cretaceous is hampered by the extreme scarcity of geological witness for this time period. In that perspective, Ashin complex rocks provide a unique window, as no other Cretaceous paleo-accretionary HP rocks are reported along the entire Zagros suture zone across 2500 km from NW Iran to the Makran region. Oceanic subduction along the northern Tethyan active margin proceeded continuously from the Lower Jurassic until the Oligocene when the Arabian continent collided with Eurasia (Agard et al., 2011; Ajirlu et al., 2016). In the meantime, the rock imprint recorded in the Ashin complex documents a steady and long-term cooling of the subduction environment from c.18 °C/km down to c.7 °C/km, which can be easily explained with the subduction of a seafloor with progressively older thermal age, at least between c.95 and 65 Ma (Angiboust et al., 2016 and Bonnet et al., 2020; see also Peacock, 2003). The paleo-geographic reconstructions shown in **Figs.15B** to **D** (from Seton et al., 2012) confirm that a progressively older and cooler oceanic lithosphere is expected between the 105 Ma thermal event and the early Cenozoic basin closure history.

The thermal pulse recorded in the Ashin complex HT unit was not identified yet in the geological record and is more challenging to link with a specific geodynamic event. The paleo-geographic reconstructions of Seton et al. (2012) and Müller & Seton (2015) predict the entrance into the subduction zone of the Neo-Tethyan mid-ocean ridge under the northern basin margin at around 120 Ma. According to Müller & Seton (2015), this ridge subduction event is inferred to have occurred at 110-120 Ma, which may, within uncertainties, be linkable to the ~105 Ma event recorded in Ashin region rocks. This event, inferred to have considerably increased the thermal gradient, may constitute one explanation, though it is (to our knowledge) not yet supported by geological observations in the region. Note that in the case of active ridge subduction, the inferred thermal gradient is expected to be much warmer than herein estimated (in the order of 40 °C/km as for instance for the southern Chile triple junction area; e.g. Lagabrielle et al., 2000). Instead, the burial of an ancient spreading ridge, which possibly had gone extinct prior to its subduction, may have provided sufficient persistent heat to trigger partial melting in the deep parts of the Zagros paleo-accretionary wedge along the northern Tethyan subduction active margin (**Fig.15E**). The warm gradient calculated for these HT rocks is also compatible with the one expected for the subduction of a very young and hence, hot oceanic lithosphere, as known for instance in the Cascades or SW Japan subduction environments. Alternatively, the subduction of a seamount derived from a plume-lithosphere interaction, as known for the nearby Siah Kuh massif (Bonnet et al., 2020) or further east in the Durkan region (Makran; Barbero et al., 2021) could also have contributed to transient heating of the subduction thermal structure at 30-40 km depth.

Another possibility is to invoke a change in the configuration of the Africa-Eurasia convergent plate boundary around 105-115 Ma as part of the "global plate reorganization event" recorded at this period (Matthews et al., 2012). Indeed, the decrease of convergence velocity documented at most convergent plate boundaries for this period would contribute to the re-equilibration of the thermal structure and a warming of subduction interface material, prior to the shift towards faster convergence rates from the Late Cretaceous to the Eocene deduced from magnetic anomalies and geological field evidence (Larson, 1991; Agard et al., 2006, 2011; Matthews et al., 2012; Olierook et al., 2020). However, such a decrease in the convergence rate between Arabia-Africa and Eurasia is not clearly documented for the time span around 105-110 Ma, because of the coeval magnetic quiet period (Granot et al., 2012). Moreover, the convergence rate does not necessarily reflect the subduction rate, which thus cannot be directly reconstructed using the Ashin complex rock record.

Last, we stress that the assembly of Cimmerian blocks is a very complex and poorly resolved geodynamic issue, and the location and activity of subduction margins in the Tethyan realm during the Cretaceous remains a matter of discussion, in particular in the light of the 105-115 Ma plate reorganization event identified recently (e.g. Matthews et al., 2012). The new constraints provided by Ashin HT rocks provide an anchor point for future paleomagnetic works and geodynamic reconstructions, helping to refine the timing of basin opening, subduction initiation and thus contributing to enhance our understanding of the geodynamic processes that shaped the northern Tethyan active margin in the Cretaceous.

## 14. CONCLUSIONS

The upper part of the Ashin complex in the Zagros Cretaceous paleo-accretionary wedge records an upper amphibolite-facies melting event (c. 650-680 °C at 1.1-1.3 GPa) that occurred at c. 104-113 Ma, leading to the formation of leucocratic veins of trondhjemitic affinity, a typical feature of partially molten mafic crust. Such a high temperature imprint requires a former warm subduction gradient (c.18 °C/km) that overprinted the rocks forming the base of an existing wedge at near 40 km depth. The origin of this thermal anomaly that has not been documented thus far, remains a matter of discussion. We favour the hypothesis of the subduction of a warm segment of the Neo-Tethyan lithosphere - such as an extinct spreading centre or a seamount chain - under the Sanandaj-Sirjan buttress. This thermal imprint left on the basally-accreted Ashin complex rocks has been followed by the underplating of another, slightly cooler unit under the thermally-overprinted Ashin HT unit, likely in the 90-100 Ma time window. Cooling down of the subduction environment to a gradient of c. 7 °C/km proceeded towards the very end of the Cretaceous, as recorded by the HP-LT overprint of previously-underplated Ashin complex material. Ashin complex basally-accreted rocks thus provide a unique window into a poorly known time period of the northern Neo-Tethyan basin evolution, with key implications for paleo-geographic reconstructions and regional geodynamic evolution.

## ACKNOWLEDGEMENTS

The four field campaigns in the Ashin region (2013-2018) would have not been possible without the logistical support from Jafar Omrani (GSI Tehran), who is warmly acknowledged. Mohammadreza Tofighi is also acknowledged for kind assistance during the last field expedition. The editorial work from Nadia Malaspina is gratefully acknowledged, as well as the careful and constructive reviews by Stefano Zanchetta and Federico Rossetti. Oona Appelt (GFZ Potsdam) is acknowledged for technical assistance with EPMA work. Gareth Seward is acknowledged for his help with BSE and EPMA analyses and Andrew Kylander-Clark for his help with LASS analyses. M. Bizimis at the Center for Elemental Mass Spectrometry at UofSC is acknowledged for considerable assistance with Lu-Hf 5mixed spike generation and aspects of the mass spectrometry. G.B. was funded by the "E-FIRE" project (NSF award OIA 1545903), with additional financial support from Bradley Hacker. J.M.M. is deeply thankful to the German Academic Exchange Service (DAAD) for a mobility grant at GFZ Potsdam. This paper benefited from thoughtful comments from A. Garcia-Casco. This study was supported by the IdEx ANR-18-IDEX-0001 as well as through an excellence research chair attributed to S.A. This is the IBERSIMS publication n. 100.

## REFERENCES

Agard, P., Monié, P., Gerber, W., Omrani, J., Molinaro, M., Meyer, B., ... & Yamato, P. (2006). Transient, synobduction exhumation of Zagros blueschists inferred from P-T, deformation, time, and kinematic constraints: Implications for Neotethyan wedge dynamics. Journal of Geophysical Research: Solid Earth, 111(B11).

Agard, P., Jolivet, L., Vrielynck, B., Burov, E., & Monie, P. (2007). Plate acceleration: the obduction trigger?. Earth and Planetary Science Letters, 258(3-4), 428-441.

Agard, P., Omrani, J., Jolivet, L., Whitechurch, H., Vrielynck, B., Spakman, W., ... & Wortel, R. (2011). Zagros orogeny: a subduction-dominated process. Geological Magazine, 148(5-6), 692-725.

Agard, P., Prigent, C., Soret, M., Dubacq, B., Guillot, S., & Deldicque, D. (2020). Slabitization: Mechanisms controlling subduction development and viscous coupling. Earth-Science Reviews, 103259.

Ajirlu, M. S., Moazzen, M., & Hajialioghli, R. (2016). Tectonic evolution of the Zagros Orogen in the realm of the Neotethys between the Central Iran and Arabian Plates: An ophiolite perspective. Central European Geology, 59(1-4), 1-27.

Alavi, M. (1994). Tectonics of the Zagros orogenic belt of Iran: new data and interpretations. Tectonophysics, 229(3-4), 211-238.

Anczkiewicz, R., Platt, J. P., Thirlwall, M. F., & Wakabayashi, J. (2004). Franciscan subduction off to a slow start: evidence from high-precision Lu–Hf garnet ages on high grade-blocks. Earth and Planetary Science Letters, 225(1-2), 147-161.

Angiboust, S., Agard, P., Glodny, J., Omrani, J., & Oncken, O. (2016). Zagros blueschists: Episodic underplating and long-lived cooling of a subduction zone. Earth and Planetary Science Letters, 443, 48-58.

Angiboust, S., Hyppolito, T., Glodny, J., Cambeses, A., Garcia-Casco, A., Calderón, M., & Juliani, C. (2017). Hot subduction in the middle Jurassic and partial melting of oceanic crust in Chilean Patagonia. Gondwana Research, 42, 104-125.

Angiboust, S., Cambeses, A., Hyppolito, T., Glodny, J., Monié, P., Calderón, M., & Juliani, C. (2018). A 100-my-long window onto mass-flow processes in the Patagonian Mesozoic subduction zone (Diego de Almagro Island, Chile). Bulletin, 130(9-10), 1439-1456.

Arfania, R., & Shahriari, S. (2009). Role of southeastern Sanandaj–Sirjan Zone in the tectonic evolution of Zagros Orogenic Belt, Iran. Island arc, 18(4), 555-576.

Arvin, M., Pan, Y., Dargahi, S., Malekizadeh, A., & Babaei, A. (2007). Petrochemistry of the Siah-Kuh granitoid stock southwest of Kerman, Iran: Implications for initiation of Neotethys subduction. Journal of Asian Earth Sciences, 30(3-4), 474-489.

Azizi, H., & Stern, R. J. (2019). Jurassic igneous rocks of the central Sanandaj–Sirjan zone (Iran) mark a propagating continental rift, not a magmatic arc. Terra Nova, 31(5), 415-423.

Barbero, E., Zaccarini, F., Delavari, M., Dolati, A., Saccani, E., Marroni, M., & Pandolfi, L. (2021). New evidence for Late Cretaceous plume-related seamounts in the Middle East sector of the Neo-Tethys: Constraints from geochemistry, petrology, and mineral chemistry of the magmatic rocks from the western Durkan Complex (Makran Accretionary Prism, SE Iran). Lithos, 396, 106228.

Barker, F. (1979). Trondhjemite: definition, environment and hypotheses of origin. In Developments in petrology (Vol. 6, pp. 1-12). Elsevier.

Berberian, M., & King, G. C. P. (1981). Towards a paleogeography and tectonic evolution of Iran. Canadian journal of earth sciences, 18(2), 210-265.

Blakey, R.C. (2008). Gondwana paleogeography from assembly to breakup—A 500 my odyssey. Geological Society of America Special Papers 441: 1-28.

Blanco-Quintero, I. F., Rojas-Agramonte, Y., García-Casco, A., Kröner, A., Mertz, D. F., Lázaro, C., ... & Renne, P. R. (2011). Timing of subduction and exhumation in a subduction channel: Evidence from slab melts from La Corea Mélange (eastern Cuba). Lithos, 127(1-2), 86-100.

Bonnet, G., Agard, P., Angiboust, S., Fournier, M., & Omrani, J. (2019). No large earthquakes in fully exposed subducted seamount. Geology, 47(5), 407-410.

Bonnet, G., Agard, P., Whitechurch, H., Fournier, M., Angiboust, S., Caron, B., & Omrani, J. (2020). Fossil seamount in southeast Zagros records intraoceanic arc to back-arc transition: New constraints for the evolution of the Neotethys. Gondwana Research, 81, 423-444.

Burg, J. P. (2018). Geology of the onshore Makran accretionary wedge: Synthesis and tectonic interpretation. Earth-Science Reviews, 185, 1210-1231.

Cherniak, D. J. (2000). Pb diffusion in rutile. Contributions to Mineralogy and Petrology, 139(2), 198-207.

Connolly, J. A. (2005). Computation of phase equilibria by linear programming: a tool for geodynamic modeling and its application to subduction zone decarbonation. Earth and Planetary Science Letters, 236(1-2), 524-541.

Davoudian, A. R., Genser, J., Neubauer, F., & Shabanian, N. (2016). 40Ar/39Ar mineral ages of eclogites from North Shahrekord in the Sanandaj–Sirjan Zone, Iran: implications for the tectonic evolution of Zagros orogen. Gondwana Research, 37, 216-240.

Delaloye, M., & Desmons, J. (1980). Ophiolites and mélange terranes in Iran: a geochronological study and its paleotectonic implications. Tectonophysics, 68(1-2), 83-111.

Dercourt, J., L. E. Ricou, and B. Vrielynck. "Atlas Tethys Palaeoenvironmental Maps Gauthier-Villars." Paris 307pp 14 (1993).

Drummond, M. S., & Defant, M. J. (1990). A model for trondhjemite-tonalite-dacite genesis and crustal growth via slab melting: Archean to modern comparisons. Journal of Geophysical Research: Solid Earth, 95(B13), 21503-21521.

Esmaeili, R., Xiao, W., Ebrahimi, M., Zhang, J. E., Zhang, Z., Abd El-Rahman, Y., ... & Aouizerat, A. (2020). Makran ophiolitic basalts (SE Iran) record Late Cretaceous Neotethys plume-ridge interaction. International Geology Review, 62(13-14), 1677-1697.

Ewing, T. A., Hermann, J., & Rubatto, D. (2013). The robustness of the Zr-in-rutile and Ti-in-zircon thermometers during high-temperature metamorphism (Ivrea-Verbano Zone, northern Italy). Contributions to Mineralogy and Petrology, 165(4), 757-779.

Ferry, J. M., & Watson, E. B. (2007). New thermodynamic models and revised calibrations for the Ti-in-zircon and Zr-in-rutile thermometers. Contributions to Mineralogy and Petrology, 154(4), 429-437.

García-Casco, A. (2007). Magmatic paragonite in trondhjemites from the Sierra del Convento mélange, Cuba. American Mineralogist, 92(7), 1232-1237.

García-Casco, A., Lázaro, C., Rojas-Agramonte, Y., Kröner, A., Torres-Roldán, R. L., Núñez, K., ... & Blanco-Quintero, I. (2008). Partial melting and counterclockwise P–T path of subducted oceanic crust (Sierra del Convento mélange, Cuba). Journal of Petrology, 49(1), 129-161.

Ghasemi, H., Juteau, T., Bellon, H., Sabzehei, M., Whitechurch, H., & Ricou, L. E. (2002). The mafic–ultramafic complex of Sikhoran (central Iran): a polygenetic ophiolite complex. Comptes Rendus Geoscience, 334(6), 431-438.

Granot, R., Dyment, J., & Gallet, Y. (2012). Geomagnetic field variability during the Cretaceous Normal Superchron. Nature Geoscience, 5(3), 220-223.

Grove, M., & Bebout, G. E. (1995). Cretaceous tectonic evolution of coastal southern California: insights from the Catalina Schist. Tectonics, 14(6), 1290-1308.

Guilmette, C., Smit, M.A., van Hinsbergen, D.J.J., Gürer, D., Corfu, F., Charette, B., Maffione, M., Rabeau, O., Savard, D. (2018). Forced subduction initiation recorded in the sole and crust of the Semail Ophiolite of Oman. Nature geosciences 11, Hassanzadeh, J., & Wernicke, B. P. (2016). The Neotethyan Sanandaj-Sirjan zone of Iran as an archetype for passive margin-arc transitions. Tectonics, 35(3), 586-621.

Hébert, R., Bezard, R., Guilmette, C., Dostal, J., Wang, C. S., & Liu, Z. F. (2012). The Indus–Yarlung Zangbo ophiolites from Nanga Parbat to Namche Barwa syntaxes, southern Tibet: First synthesis of petrology, geochemistry, and geochronology with incidences on geodynamic reconstructions of Neo-Tethys. Gondwana Research, 22(2), 377-397.

Kananian, A., Sarjoughian, F., Nadimi, A., Ahmadian, J., & Ling, W. (2014). Geochemical characteristics of the Kuh-e Dom intrusion, Urumieh–Dokhtar Magmatic Arc (Iran): Implications for source regions and magmatic evolution. Journal of Asian Earth Sciences, 90, 137-148.

Kohn, M. J. (2020). A refined zirconium-in-rutile thermometer. American Mineralogist: Journal of Earth and Planetary Materials, 105(6), 963-971.

Krebs, M., Maresch, W. V., Schertl, H. P., Münker, C., Baumann, A., Draper, G., ... & Trapp, E. (2008). The dynamics of intra-oceanic subduction zones: a direct comparison between fossil petrological evidence (Rio San Juan Complex, Dominican Republic) and numerical simulation. Lithos, 103(1-2), 106-137.

Lagabrielle, Y., Guivel, C., Maury, R. C., Bourgois, J., Fourcade, S., & Martin, H. (2000). Magmatic–tectonic effects of high thermal regime at the site of active ridge subduction: the Chile Triple Junction model. Tectonophysics, 326(3-4), 255-268.

Larson, R. L. (1991). Latest pulse of Earth: Evidence for a mid-Cretaceous superplume. Geology, 19(6), 547-550.

Lázaro, C., Blanco-Quintero, I. F., Marchesi, C., Bosch, D., Rojas-Agramonte, Y., & García-Casco, A. (2011). The imprint of subduction fluids on subducted MORB-derived melts (Sierra del Convento Mélange, Cuba). Lithos, 126(3-4), 341-354.

Li, W. C., Chen, R. X., Zheng, Y. F., Tang, H., & Hu, Z. (2016). Two episodes of partial melting in ultrahigh-pressure migmatites from deeply subducted continental crust in the Sulu orogen, China. Bulletin, 128(9-10), 1521-1542.

Li, S. M., Wang, Q., Zhu, D. C., Stern, R. J., Cawood, P. A., Sui, Q. L., & Zhao, Z. (2018). One or two Early Cretaceous arc systems in the Lhasa Terrane, southern Tibet. Journal of Geophysical Research: Solid Earth, 123(5), 3391-3413.

Mahoney, J. J., Graham, D. W., Christie, D. M., Johnson, K. T. M., Hall, L. S., & Vonderhaar, D. L. (2002). Between a hotspot and a cold spot: isotopic variation in the Southeast Indian Ridge asthenosphere, 86 E–118 E. Journal of Petrology, 43(7), 1155-1176.

Matthews, K. J., Seton, M., & Müller, R. D. (2012). A global-scale plate reorganization event at 105− 100 Ma. Earth and Planetary Science Letters, 355, 283-298.

McCall, G. J. H. (1997). The geotectonic history of the Makran and adjacent areas of southern Iran. Journal of Asian Earth Sciences, 15(6), 517-531.

Moyen, J., & Stevens, G. (2006). Experimental constraints on TTG petrogenesis: implications for Archean geodynamics. Geophysical Monograph-American Geophysical Union, 164, 149

Müller, R. D., & Seton, M. (2015). Paleophysiography of ocean basins. Encyclopedia of Marine Geosciences.

Muñoz-Montecinos, J., Angiboust, S., Garcia-Casco, A., Glodny, J., & Bebout, G. (2021). Episodic hydrofracturing and large-scale flushing along deep subduction interfaces: Implications for fluid transfer and carbon recycling (Zagros Orogen, southeastern Iran). Chemical Geology, 571, 120173.

O'Connor, J. T. (1965). A classification for quartz-rich igneous rocks. Geol. Surv. Prof. Pap, 525, 79.

Olierook, H. K., Jourdan, F., Whittaker, J. M., Merle, R. E., Jiang, Q., Pourteau, A., & Doucet, L. S. (2020). Timing and causes of the mid-Cretaceous global plate reorganization event. Earth and Planetary Science Letters, 534, 116071.

Omrani, J. (2008). The geodynamic evolution of Zagros: Tectonic and petrological constraints from the internal zones (Doctoral dissertation, Paris 6).

Peacock, S. M. (2003). Thermal structure and metamorphic evolution of subducting slabs. Geophysical Monograph-American Geophysical Union, 138, 7-22.

Pearce, J. A. (2008). Geochemical fingerprinting of oceanic basalts with applications to ophiolite classification and the search for Archean oceanic crust. Lithos, 100(1-4), 14-48.

Penniston-Dorland, S. C., Kohn, M. J., & Piccoli, P. M. (2018). A mélange of subduction temperatures: Evidence from Zr-in-rutile thermometry for strengthening of the subduction interface. Earth and Planetary Science Letters, 482, 525-535.

Pourteau, A., Scherer, E. E., Schorn, S., Bast, R., Schmidt, A., & Ebert, L. (2019). Thermal evolution of an ancient subduction interface revealed by Lu–Hf garnet geochronology, Halilbağı Complex (Anatolia). Geoscience Frontiers, 10(1), 127-148.

Rapp, R. P., Watson, E. B., & Miller, C. F. (1991). Partial melting of amphibolite/eclogite and the origin of Archean trondhjemites and tonalites. Precambrian Research, 51(1-4), 1-25.

Rodriguez, M., Arnould, M., Coltice, N., & Soret, M. (2021). Long-term evolution of a plume-induced subduction in the Neotethys realm. Earth and Planetary Science Letters, 561, 116798.

Rossetti, F., Nasrabady, M., Vignaroli, G., Theye, T., Gerdes, A., Razavi, M. H., & Vaziri, H. M. (2010). Early Cretaceous migmatitic mafic granulites from the Sabzevar range (NE Iran): implications for the closure of the Mesozoic peri-Tethyan oceans in central Iran. Terra Nova, 22(1), 26-34.

Rossetti, F., Monié, P., Nasrabady, M., Theye, T., Lucci, F., & Saadat, M. (2017). Early Carboniferous subduction-zone metamorphism preserved within the Palaeo-Tethyan Rasht ophiolites (western Alborz, Iran). Journal of the Geological Society, 174(4), 741-758.

Rubatto, D. (2002). Zircon trace element geochemistry: partitioning with garnet and the link between U–Pb ages and metamorphism. Chemical geology, 184(1-2), 123-138.

Sabzehei, M. (1974). Les Mélanges ophiolitiques de la région d'Esfandagheh (Iran méridional): étude pétrologique et structurale, interprétation dans le cadre iranien (Doctoral dissertation, Université Scientifique et Médicale de Grenoble).

Saccani, E., Delavari, M., Dolati, A., Marroni, M., Pandolfi, L., Chiari, M., & Barbero, E. (2018). New insights into the geodynamics of Neo-Tethys in the Makran area: Evidence from age and petrology of ophiolites from the Coloured Mélange Complex (SE Iran). Gondwana Research, 62, 306-327.

Şengör, A. M. C., Altıner, D., Cin, A., Ustaömer, T., & Hsü, K. J. (1988). Origin and assembly of the Tethyside orogenic collage at the expense of Gondwana Land. Geological Society, London, Special Publications, 37(1), 119-181.

Seton, M., Müller, R. D., Zahirovic, S., Gaina, C., Torsvik, T., Shephard, G., ... & Chandler, M. (2012). Global continental and ocean basin reconstructions since 200 Ma. Earth-Science Reviews, 113(3-4), 212-270.

Shafaii Moghadam, H.S., & Stern, R. J. (2011). Geodynamic evolution of Upper Cretaceous Zagros ophiolites: formation of oceanic lithosphere above a nascent subduction zone. Geological Magazine, 148(5-6), 762-801.

Shafaii Moghadam, H.S., Bröcker, M., Griffin, W. L., Li, X. H., Chen, R. X., & O'Reilly, S. Y. (2017). Subduction, high-P metamorphism, and collision fingerprints in South Iran: Constraints from zircon U-Pb and mica Rb-Sr geochronology. Geochemistry, Geophysics, Geosystems, 18(1), 306-332.

Söderlund, U., Patchett, P.J., Vervoort, J.D., Isachsen, C.E. (2004). The 176Lu decay constant determined by Lu-Hf and U-Pb isotope systematics of Precambrian mafic intrusions, Earth and Planetary Science Letters, 219, 311-324.

Sorensen, S. S., & Barton, M. D. (1987). Metasomatism and partial melting in a subduction complex Catalina Schist, southern California. Geology, 15(2), 115-118.

Stampfli, Gérard M., and G. D. Borel. "A plate tectonic model for the Paleozoic and Mesozoic constrained by dynamic plate boundaries and restored synthetic oceanic isochrons." Earth and Planetary Science Letters 196.1-2 (2002): 17-33.

Stern, R. J. (2002). Subduction zones. Reviews of geophysics, 40(4), 3-1.

Tomkins, H. S., Powell, R., & Ellis, D. J. (2007). The pressure dependence of the zirconium-in-rutile thermometer. Journal of metamorphic Geology, 25(6), 703-713.

Vervoort, J.D. & Blichert-Toft, J. (1999). Evolution of the depleted mantle: Hf isotope evidence from juvenile rocks through time. Geochimica et Cosmochimica Acta, 63, 533-556.

Vielzeuf, D., & Schmidt, M. W. (2001). Melting relations in hydrous systems revisited: application to metapelites, metagreywackes and metabasalts. Contributions to Mineralogy and Petrology, 141(3), 251.

Yang, G., & Dilek, Y. (2015). OIB-and P-type ophiolites along the Yarlung-Zangbo Suture Zone (YZSZ), Southern Tibet: Poly-Phase melt history and mantle sources of the Neotethyan oceanic lithosphere. Episodes, 38(4), 250-265.

Zack, T., Moraes, R., & Kronz, A. (2004). Temperature dependence of Zr in rutile: empirical calibration of a rutile thermometer. Contributions to Mineralogy and Petrology, 148(4), 471-488.

# SUPPLEMENTARY MATERIAL

## APPENDIX A. ANALYTICAL METHODS

### A.1 Electron microprobe measurements

Petrological investigations were conducted on a set of 14 representative samples localized on **Fig.1C** and **Table S1**. Electron probe microanalyses were acquired at the GFZ Potsdam with a GEOL-JXA8230 and at the Department of Earth Sciences, University of California Santa Barbara, on a Cameca SX-100 machine under common analytical conditions (15 Kv, 20 to 10 nA, wavelength-dispersive spectroscopy mode) using a 5 µm beam. Standards used for the calibration were as follows: orthoclase (Al, Si, K), fluorite (F), rutile (Ti), $Cr_2O_3$ (Cr), wollastonite (Ca), tugtupite (Cl), albite (Na), MgO (Mg), $Fe_2O_3$ (Fe) and rhodonite (Mn). Elemental X-ray maps were performed on the same instruments with a step size of 5 and 20 µm and a dwell time of 20 ms. The resulting X-ray maps were processed using the software DWImager (Garcia-Casco, 2007). In order to highlight minerals and textures of interest, some mineral phases were masked out, and the colour images of the phases of interest were overlain onto a grayscale-image base-layer. Representative major element mineral analyses are provided in **Table S2.**

### A.2 Whole rock major and trace elements geochemistry

Six representative leucocratic veins and ten amphibolites were processed for whole rock major and trace element determinations using X-ray fluorescence (XRF) and inductively coupled plasma mass spectroscopy (ICP-MS) at the Centre for Scientific Instrumentation of the University of Granada (CIC-UGR). XRF major element analyses were performed after melting using a lithium tetraborate fusion flux. Typical analytical accuracy was better than ± 1.5% for an analyte concentration of 10 wt. %. Zirconium was determined by X-ray fluorescence on the same disks, with a precision better than ± 4% for 100 µg/g of Zr. ICP-MS measurements were performed after $HNO_3$+HF digestion of 0.1 g of sample powder in a Teflon-lined vessel at ~180 °C and 200 psi for 30 min, evaporation to dryness, and subsequent dissolution in 100 ml of 4 vol.% $HNO_3$. Instrument measurements were carried out in triplicate with a PE SCIEX ELAN- 8000 spectrometer using rhodium as an internal standard. Precision determined from standards WSE, BR and AGV run as unknowns, was better than ± 2% and ± 5% for analyte concentrations of 50 and 5 µg/g, respectively. The results are presented in **Table S3**.

### A.3 Rutile LA-ICP-MS measurements

In situ U–Pb and trace-element analyses of rutile were performed using the laser ablation split-stream (LASS) facility at the University of California, Santa Barbara (USA). The LASS system combines a Cetac 193-nm ArF Excimer laser and Hel-Ex2 ablation cell with a Nu Instruments Plasma HR-ES multi-collector ICP-MS for collecting U-Th-Pb data and an Agilent 7700S quadrupole ICP-MS for collecting major and trace element data. Methods used in this study follow those outlined by Kylander-Clark et al. (2013). Rutile grains were analysed in situ in thin sections and from separated crystal mounts. Rutile was ablated using a variable beam diameter, depending on the grain size of the sample, of 35 µm (for SO1866) or 50 µm spots (for all other samples), at 4 Hz repetition rate for 60 shots at a laser fluence of 1 J/cm$^2$, after two pre-ablation shots at 50% laser power used to remove surface contamination. U–Pb data reduction, including corrections for baseline, instrumental drift, mass bias, down-hole fractionation and uncorrected age calculations were carried out using the Iolite v. 2.5 (Paton et al., 2011), and error correlations were recalculated after Schmitz and Schoene (2007). Analyses of unknowns were bracketed (once every ~8 unknowns) by analyses of matrix-matched reference material Kragerø rutile (~1090 Ma ID-TIMS date; Luvizotto et al., 2009; Bracciali et al., 2013). Secondary rutile reference material R9826J (381.9 ± 1.1 Ma TIMS date; Kylander-Clark et al., 2008), Wodgina (2845.4 ± 0.5 Ma Tera-Wasserburg Concordia date; Ewing, 2011) were analysed concurrently (once every ~16 unknowns) and treated as unknowns to assess accuracy and precision. The uncertainty on isotopic ratios includes the internal uncertainty determined by Iolite to which a systematic percentage of uncertainty was added to ensure that the weighted mean of isotopic ratios of secondary standard R9826J analyses have a MSWD of 1. During the course of the study, we obtained ages of 386.0 ± 2.4 Ma for R9826J (n=20), and 2777.9 ± 14.6 Ma for Wodgina (n=20), within 1.1% and 2.4% of the reference values, respectively. All unknowns were additionally bracketed by analyses of international glass standard BHVO2G (Jochum et al., 2005), that was used as a primary standard for trace elements, using $^{47}$Ti as the internal standard element and an assumed concentration of 59.94 wt.% Ti in rutile. For these samples, U-Pb isotopic analyses were displayed with 95%-confidence error ellipses in Tera-Wasserburg diagrams. Discordia isochron ages were calculated with IsoplotR (Vermeesch, 2018) using the least-square “York” method. In order to decipher the span of ages covered, isochrons were anchored to the common $^{207}$Pb/$^{206}$Pb value at 100 Ma (Stacey & Kramers, 1975).

### A.4 Zircon LA-ICP-MS and SHRIMP measurements

Zircon crystals were separated using panning, first in water and then in ethanol. This was followed by magnetic extraction of Fe-rich minerals with a NdFeB permanent magnet. Finally, zircons were handpicked using a binocular microscope. The zircons were cast on “megamounts”, i.e. 35 mm epoxy discs fixed on the front of a mount holder so that no metallic parts or surface discontinuities faced the secondary ions extraction plate. The crystals were carefully studied with optical (reflected and transmitted light) and scanning electronic microscopy (backscattering and cathodoluminescence) prior to laser ablation inductively coupled plasma mass spectroscopy (LA-ICP-MS) and SHRIMP analyses.

Trace element analyses were done at the CIC-UGR LA-ICP-MS laboratory using a Perkin Elmer NexION 350X ICP-MS coupled to a New Wave Research NR 213 laser ablation system. The analyses were performed on the same mounts used for isotope analyses using the NIST-610 glass as an external standard, which was measured after every six unknowns. Spots to be analyzed were pre-ablated for 15 seconds with a laser fluency of 2.5 J cm$^{-2}$, and then ablated for 60 seconds with a laser fluency of 7.5 J cm$^{-2}$. A blank, measured in the same conditions but with zero laser energy, preceded every measurement. Data reduction was done using an in-house software written in the STATA™ programming language.

Zircon crystals were analysed at the CIC-UGR with the IBERSIMS SHRIMP IIe/mc ion microprobe for U-Th-Pb following the method described by Williams & Claesson (1987). The mount was coated with a c. 12 nm thick gold layer. Each spot was rasterized with the primary beam for 120 s prior to analysis and then analysed for 6 scans following the isotope peak sequence $^{196}$Zr$_2$O, $^{204}$Pb, $^{204.1}$background, $^{206}$Pb, $^{207}$Pb, $^{208}$Pb, $^{238}$U, $^{248}$ThO, $^{254}$UO. Every peak of every scan was measured sequentially 10 times with the following total counting times per scan: 2 seconds for mass 196; 5 seconds for masses 238, 248, and 254; 15 seconds for masses 204, 206, and 208; and 20 seconds for mass 207. The primary beam, composed of $^{16}$O$^{-16}$O+, was set to an intensity of about 5 nA, with two Köhler apertures: (1) at 120 μm and (2) at 70 μm, which generated 17 × 20 and 9 × 12 μm elliptical spots on the target to analyse cores and rims respectively (see Zircon dating results section). The secondary beam exit slit was fixed at 80 microns, achieving a resolution of about 5000 at 1% peak height. All calibration procedures were performed on the standards included on the same mount. Mass calibration was done on the REG zircon (ca. 2.5 Ga, very high U, Th and common lead content). The analytical session started by measuring the SL13 zircon (Claoue-Long et al., 1995), which was used as a concentration standard (238 ppm U). The TEMORA zircon (416.8 ± 1.1 Ma; Black et al., 2003), used as an isotope ratios standard, was then measured after every 4 unknowns. Data reduction was done with the SHRIMPTOOLS software (available from www.ugr.es/~fbea), which is a new implementation of the PRAWN software originally developed for the SHRIMP. Uncertainties are reported at the 95% confidence interval ($\approx 2\sigma$). Standard uncertainties (95% C.I) on the 37 replicates of the TEMORA standard measured during the analytical session were ± 0.35% for 206Pb/238U and ± 0.83 % for 207Pb/206Pb. The resulting ages, isotopic ratios and element concentrations are presented in **Table S5**.

### A.5 Lu-Hf garnet analysis

A garnet micaschist from the HT unit (SO1803a) has been selected for Lu-Hf dating according to the following criteria: (i) the sample contains sufficiently large garnet crystals; (ii) the garnet crystals are fresh (e.g., no retrograde replacement); (iii) the sample preserves its peak assemblage with minor evidence of retrogression. The methodology for initial preparation for garnet geochronology broadly follows that described by Dragovic et al. (2012). The sample was split into two sub-volumes; one for garnet separation and the other for whole rock/matrix preparation. The first sub-volume was hand-crushed using an agate mortar and pestle, sieved to between 74 and 149 μm grain size (100-200 mesh size), and run through a Frantz magnetic separator in order to remove most of the non-garnet minerals. The resultant garnet separate was divided into several fractions of ~100-150 mg each for subsequent dissolution and clean chemistry. A "matrix" sample was obtained by physical separation of garnet porphyroblasts from the whole rock sub-volume. Both the matrix and whole rock were powdered using an agate mortar and pestle. All samples subsequently underwent a full dissolution procedure. Aliquots of the whole rock and matrix were digested using a 4:1 $HF/HNO_3$ solution in a Parr bomb (i.e. a high-pressure, steel-jacketed Teflon vessel) for 7 days. Additional aliquots of the whole rock and matrix, along with the garnet separates were also digested by a "tabletop" technique. This approach first involves treatment in a concentrated HF/1.5N HCl solution at 120°C. This is performed until few visible grains remain (importantly, the refractory and Hf-rich minerals zircon and rutile remain undissolved and thus do not affect isotopic analyses). Samples are then redissolved in 2:1 concentrated $HNO_3$/1.5N HCl to remove secondary fluorides. All samples were then equilibrated with either of two, in-house mixed $^{176}$Lu-$^{180}$Hf spikes (garnet fractions vs. rock matrix/whole rock) appropriately chosen for the (elemental) Lu/Hf ratio of the samples. Following this, a two-step column chromatography procedure was performed to extract high purity Lu and Hf separates, modified after the methods of Bast et al. (2015).

Analyses were performed at the Center for Elemental Mass Spectrometry (CEMS) at the School of the Earth, Ocean and Environment, University of South Carolina, using a Thermo-Fisher Neptune Plus multi-collector inductively coupled plasma mass spectrometer (MC-ICP-MS) with an Apex Omega desolvating nebulizer. The $^{176}$Lu/$^{175}$Lu was determined following Vervoort et al. (2004) based on the observation that the Yb-isotope mass fractionation on the instrument biased relative to the Lu-isotope mass fractionation. The reproducibility of the calculated natural $^{176}$Lu/$^{175}$Lu (taken as $^{176}$Lu/$^{175}$Lu =

0.02655) is tested in different Lu/Yb elemental mixtures at the beginning of each analytical session. We used $^{173}$Yb/$^{171}$Yb = 1.129197 for mass fractionation and calculated the $^{176}$Yb contribution to the $^{176}$Lu signal using a $^{176}$Yb/$^{173}$Yb (natural) value of 0.793045. Based on a plot of $^{176}$Yb-interference- and fractionation-corrected $^{176}$Lu/$^{177}$Lu vs. $^{173}$Yb/$^{175}$Lu (proportional to elemental Yb/Lu), we determined an instrumental mass bias factor of 0.9997 on the $^{176}$Yb/$^{173}$Yb ratio upon which corrected $^{176}$Lu/$^{177}$Lu ratios remain constant for a range of added Yb. This mass bias factor is instrument- and introduction system-dependent and relates to the transmission of each isotope beam through the instrument, but varies between 0.9996 and 0.9998, long-term, at CEMS. The $^{176}$Hf/$^{177}$Hf and Hf concentrations were determined. The $^{179}$Hf/$^{177}$Hf value of 0.7325 was used for mass fractionation correction. External reproducibility on 30-ng runs of an in-house Hf standard elemental solution during the analytical session was 0.25 $\varepsilon_{\mathrm{Hf}}$ units (n= 10). Lastly, Lu and Hf concentrations were determined by isotope dilution, and $^{176}$Lu/$^{177}$Hf ratios were calculated from that data. The resulting isotopic data and ages are presented in **Table S4**.

### A.6 Additional information for the pseudosection modelling approach

We used the following list of Perple_X solid solution models: feldspar (Fuhrman and Lindsley, 1988), clinopyroxene (Holland and Powell, 1996), chlorite (Holland et al., 1998), orthopyroxene (Powell and Holland, 1999), ilmenite (Ti-phases, White et al. 2000), amphibole (Dale et al, 2005), melt, garnet and biotite (White et al, 2007) and white mica (Smye et al., 2010). The choice of this list is motivated and justified by the consistency of results obtained in a previous study on partially molten MORB rocks (Angiboust et al., 2017) for a geological problem largely similar to the current investigation. Modelling is run using the ds5 thermodynamic database (Holland and Powell, 1998; updated in 2002).

## Supplementary References

Bast, R., Scherer, E.E., Sprung, P., Fischer-Gödde, M., Stracke, A., Mezger, K. (2015). A rapid and efficient ion-exchange chromatography for Lu-Hf, Sm-Nd, and Rb-Sr geochronology and the routine isotope of sub-ng amounts of Hf by MC-ICP-MS. Journal of Analytical and Atomic Spectrometry, 30, 2323.

Black, L. P., Kamo, S. L., Allen, C. M., Aleinikoff, J. N., Davis, D. W., Korsch, R. J. & Foudoulis, C. (2003). TEMORA 1: a new zircon standard for Phanerozoic U–Pb geochronology. Chemical Geology 200(1-2), 155-170.

Bracciali, L., Parrish, R. R., Horstwood, M. S., Condon, D. J., & Najman, Y. (2013). UPb LA-(MC)-ICP-MS dating of rutile: New reference materials and applications to sedimentary provenance. Chemical Geology, 347, 82-101.

Claoue-Long, J., Compston, W., Roberts, J. & Fanning, C.M. (1995). Two carboniferous ages: a comparison of SHRIMP zircon dating with conventional zircon ages & 40Ar/39Ar analysis. In: Berggren, W.A., Kent, D.V., Aubry, M.P., Hardenbol, J. (eds) Geochronology, Time Scales & Stratigraphic Correlation. SEPM Special Publication 54, 1-22.

Dale, J., Powell, R., White, R. W., Elmer, F. L., & Holland, T. J. B. (2005). A thermodynamic model for Ca–Na clinoamphiboles in Na2O–CaO–FeO–MgO–Al2O3–SiO2–H2O–O for petrological calculations. Journal of Metamorphic Geology, 23(8), 771-791.

Dragovic, B., Samanta, L., Baxter, E.F., Selverstone, J. (2012). Using garnet to constrain the duration and rate of water-releasing metamorphic reactions during subduction: An example from Sifnos, Greece. Chemical Geology, 314-317, 9-22.

Ewing, T. A. (2011). Hf isotope analysis and U-Pb geochronology of rutile: Technique development and application to a lower crustal section (Ivrea-Verbano Zone, Italy).

Fuhrman, M. L., & Lindsley, D. H. (1988). Ternary-feldspar modeling and thermometry. American mineralogist, 73(3-4), 201-215.

Holland, T., & Powell, R. (1996). Thermodynamics of order-disorder in minerals: II. Symmetric formalism applied to solid solutions. American Mineralogist, 81(11-12), 1425-1437.

Holland, T., Baker, J., & Powell, R. (1998). Mixing properties and activity-composition relationships of chlorites in the system MgO-FeO-Al2O3-SiO2-H2O. European Journal of Mineralogy, 395-406.

Holland, T. J. B., & Powell, R. T. J. B. (1998). An internally consistent thermodynamic data set for phases of petrological interest. Journal of metamorphic Geology, 16(3), 309-343.

Jochum, K. P., Willbold, M., Raczek, I., Stoll, B., & Herwig, K. (2005). Chemical Characterisation of the USGS Reference Glasses GSA-1G, GSC-1G, GSD-1G, GSE-1G, BCR-2G, BHVO-2G and BIR-1G Using EPMA, ID-TIMS, ID-ICP-MS and LA-ICP-MS. Geostandards and Geoanalytical Research, 29(3), 285-302.

Kylander-Clark, A. R. C., Hacker, B. R., & Mattinson, J. M. (2008). Slow exhumation of UHP terranes: titanite and rutile ages of the Western Gneiss Region, Norway. Earth and Planetary Science Letters, 272(3-4), 531-540.

Kylander-Clark, A. R., Hacker, B. R., & Cottle, J. M. (2013). Laser-ablation split-stream ICP petrochronology. Chemical Geology, 345, 99-112.

Luvizotto, G. L., Zack, T., Meyer, H. P., Ludwig, T., Triebold, S., Kronz, A., ... & von Eynatten, H. (2009). Rutile crystals as potential trace element and isotope mineral standards for microanalysis. Chemical Geology, 261(3-4), 346-369.

Paton, C., Hellstrom, J., Paul, B., Woodhead, J., & Hergt, J. (2011). Iolite: Freeware for the visualisation and processing of mass spectrometric data. Journal of Analytical Atomic Spectrometry, 26(12), 2508-2518.

Powell, R., & Holland, T. (1999). Relating formulations of the thermodynamics of mineral solid solutions; activity modeling of pyroxenes, amphiboles, and micas. American mineralogist, 84(1-2), 1-14.

Schmitz, M. D., & Schoene, B. (2007). Derivation of isotope ratios, errors, and error correlations for U-Pb geochronology using 205Pb-235U-(233U)-spiked isotope dilution thermal ionization mass spectrometric data. Geochemistry, Geophysics, Geosystems, 8(8).

Smye, A. J., Greenwood, L. V., & Holland, T. J. B. (2010). Garnet–chloritoid–kyanite assemblages: eclogite facies indicators of subduction constraints in orogenic belts. Journal of Metamorphic Geology, 28(7), 753-768.

Stacey, J. T., & Kramers, 1. (1975). Approximation of terrestrial lead isotope evolution by a two-stage model. Earth and planetary science letters, 26(2), 207-221.

Vermeesch, P. (2018). IsoplotR: A free and open toolbox for geochronology. Geoscience Frontiers, 9(5), 1479-1493.

Vervoort, J.D., Patchett, P.J., Sönderlund, U., Baker, M. (2004). Isotopic composition of Yb and the determination of Lu concentrations and Lu/Hf ratios by isotope dilution using MC-ICPMS. Geochemistry, Geophysics, Geosystems, 5 (11).

White, R. W., Powell, R., Holland, T. J. B., & Worley, B. A. (2000). The effect of TiO2 and Fe2O3 on metapelitic assemblages at greenschist and amphibolite facies conditions: mineral equilibria calculations in the system K2O-FeO-MgO-Al2O3-SiO2-H2O-TiO2-Fe2O3. Journal of Metamorphic Geology, 18(5), 497-511.

White, R. W., Powell, R., & Holland, T. J. B. (2007). Progress relating to calculation of partial melting equilibria for metapelites. Journal of metamorphic Geology, 25(5), 511-527.

Williams, I. S. & Claesson, S. (1987). Isotopic evidence for the Precambrian provenance and Caledonian metamorphism of high grade paragneisses from the Seve Nappes, Scandinavian Caledonides. Contributions to mineralogy and petrology 97(2), 205-217.

## SUPPLEMENTARY FIGURE AND TABLE CAPTIONS

**Figure S1**: Mineral chemistry diagrams for epidote (**A**), white mica **(B** to **D**) and zircon (**E** and **F**).
**Figure S2**: Additional data for sample SO1317. **A**. The hand specimen section for overview. **B**. Cathodoluminescence images showing the structure of a leucocratic domain. **C**. A grey-scale colored cathodoluminescence image of a restitic domain, showing the foliation-parallel leucocratic veinlets separating Hbl-rich areas.
**Figure S3**. Photomicrograph **(A**) and X-ray maps (**B**) of a garnet micaschist from the Ashin MT unit.
**Figure S4**. Phase abundances relative to $H_2O$ variations at fixed PT conditions (1.2 GPa and 650 °C).
**Table S1**: Summary of petrographic observations for the set of selected samples for this study as well as GPS sampling coordinates.
**Table S2**: Selected electron probe mineral analyses and associated structural formulae calculations.
**Table S3**: Whole-rock geochemical data (major and trace elements) for the host amphibolites and leucosomes.
**Table S4.** Lu-Hf isotopic data and garnet age from HT garnet micaschist sample SO1803a.
**Table S5 :** U–Pb SHRIMP data for leucosome sample SO1805C, d(%) = 100 × (1 − 206 / 238 age / 207 / 235 age); f206% = (common 206Pb / total 206Pb) × 100. All errors are at 95%. Trace element data of studied zircons. Ti-in-zircon temperatures calculated after Ferry & Watson (2007).